



UNICAMP

UNIVERSIDADE DE CAMPINAS
Instituto de Física Gleb Wataghin

MARINA REGGIANI GUZZO

**Study of the effect of contamination on the liquid argon
scintillation light in the ProtoDUNE-SP experiment**

Estudo do efeito da contaminação na luz de cintilação do
argônio líquido no experimento ProtoDUNE-SP

Campinas

2019

Marina Reggiani Guzzo

**Study of the effect of contamination on the liquid argon
scintillation light in the ProtoDUNE-SP experiment**

Estudo do efeito da contaminação na luz de cintilação do
argônio líquido no experimento ProtoDUNE-SP

Dissertação apresentada ao Instituto de Física
"Gleb Wataghin" da Universidade Estadual de
Campinas como parte dos requisitos exigidos
para a obtenção do título de Mestra em Física,
na área de Física Aplicada.

Dissertation presented to the "Gleb
Wataghin" Institute of Physics of the Uni-
versity of Campinas in partial fulfillment of
the requirements for the degree of Master in
Physics, in the area of Applied Physics.

Advisor/Orientador: Ettore Segreto

Este exemplar corresponde à versão fi-
nal da dissertação defendida pela aluna
Marina Reggiani Guzzo e orientado pelo
Prof. Dr. Ettore Segreto.

CAMPINAS

2019

Ficha catalográfica
Universidade Estadual de Campinas
Biblioteca do Instituto de Física Gleb Wataghin
Lucimeire de Oliveira Silva da Rocha - CRB 8/9174

G994s Guzzo, Marina Reggiani, 1994-
Study of the effect of contamination on the liquid argon scintillation light in the ProtoDUNE-SP experiment / Marina Reggiani Guzzo. – Campinas, SP : [s.n.], 2019.

Orientador: Ettore Segreto.
Dissertação (mestrado) – Universidade Estadual de Campinas, Instituto de Física Gleb Wataghin.

1. Neutrinos. 2. Contadores de cintilações. 3. Argônio líquido. I. Segreto, Ettore, 1973-. II. Universidade Estadual de Campinas. Instituto de Física Gleb Wataghin. III. Título.

Informações para Biblioteca Digital

Título em outro idioma: Estudo do efeito da contaminação na luz de cintilação do argônio líquido no experimento ProtoDUNE-SP

Palavras-chave em inglês:

Neutrinos
Scintillation counters
Liquid argon

Área de concentração: Física Aplicada

Titulação: Mestra em Física

Banca examinadora:

Ettore Segreto [Orientador]
Ronald Cintra Shellard
Carola Dobrigkeit Chinellato

Data de defesa: 10-06-2019

Programa de Pós-Graduação: Física

Identificação e informações acadêmicas do(a) aluno(a)
- ORCID do autor: <https://orcid.org/0000-0002-6169-2982>
- Currículo Lattes do autor: <http://lattes.cnpq.br/4914983851683351>



MEMBROS DA COMISSÃO JULGADORA DA DISSERTAÇÃO DE MESTRADO DE **MARINA REGGIANI GUZZO - 136961** APRESENTADA E APROVADA AO INSTITUTO DE FÍSICA “GLEB WATAGHIN”, DA UNIVERSIDADE ESTADUAL DE CAMPINAS, EM 10 / 06 / 2019.

COMISSÃO JULGADORA:

- Prof. Dr. Ettore Segreto – Orientador – DRCC/IFGW/UNICAMP
- Prof. Dr. Ronald Cintra Shellard – CBPF
- Profa. Dra. Carola Dobrigkeit Chinellato – DRCC/IFGW/UNICAMP

OBS.: Informo que as assinaturas dos respectivos professores membros da banca constam na ata de defesa já juntada no processo vida acadêmica do aluno.

CAMPINAS
2019

"A gente leva da vida a vida que a gente leva."

- Tom Jobim

Acknowledgements

First, I would like to thank my supervisor, Ettore Segreto, who guided me throughout my studies. I would also like to thank Ana Amelia Machado and all the students in the UNICAMP group which always brighten my days with their presences in the laboratory.

I would also like to thank Ettore Segreto, Anderson Fauth and Jennifer Raaf for the support during the application process in the Neutrino Physics Center Fellowship Program, as well as my special thanks to Alexander Himmel for having me as a student during my stay at Fermilab.

I would also like to thank Bryan Ramson, Dante Totani and Flavio Cavanna for their hard work to do the calibration of the photon-detection system. Thank you Jake Calcutt for sharing your knowledge about the particle beam. I would also like to thank all DUNE Photon Detection Consortium.

I would also like to thank my parents, Marcelo Moraes Guzzo and Norma Reggiani, and my brother, Tomás Reggiani Guzzo, for guiding me professional and personally. To all my friends that have always been there for me, in particular Thomas Joseph Carroll III, Laryssa Abdala, Henrique Vieira de Souza, Vitor Barroso Silveira, and Luisa Rodrigues Vilarta. Thank you for all your support, crucial for me to be here.

Finally, I recognize the importance of the financial support given to me the past two years for the conclusion of the present work. This study was financed in part by the Coordenação de Aperfeiçoamento de Pessoal de Nível Superior - Brasil (CAPES) - Finance Code 001. I thank the Conselho Nacional de Desenvolvimento Científico e Tecnológico (CNPq) for financially supporting my masters studies at UNICAMP - Finance Code 132440/2017-2. I thank the Fundação de Amparo à Pesquisa do Estado de São Paulo (FAPESP) for financially supporting the ARAPUCA project - grants 2016/01106-5. Last but not least, I thank the Neutrino Physics Center Program for giving me the opportunity to work at Fermilab, close to the

ACKNOWLEDGEMENTS

experts in my field.

Resumo

DUNE é um dos experimentos mais importantes na área de física de neutrinos que pretende estudar questões em aberto sobre neutrinos, neutrinos de supernovas e decaimento do próton. O experimento ProtoDUNE-SP é um protótipo de grande escala do experimento DUNE instalado no CERN que vem tomando dados desde setembro de 2018. Ambos os experimentos, DUNE e ProtoDUNE-SP, utilizam a técnica experimental de detecção Liquid Argon Time Projection Chamber (LArTPC). O estudo do presente trabalho teve como foco a estimativa do comprimento de espalhamento Rayleigh no experimento ProtoDUNE-SP. A análise dos dados indica um comprimento de espalhamento Rayleigh de aproximadamente 97^{+25}_{-15} cm, que coincide com o valor estimado analiticamente.

Palavras-chave: Neutrinos; Contadores de cintilações; Argônio líquido.

Abstract

DUNE is one of the most important experiments in the field of neutrino physics aiming to study open questions about neutrinos, supernova neutrinos, and proton decay. The experiment ProtoDUNE-SP is the large-scale prototype of the DUNE experiment. ProtoDUNE-SP is installed at CERN and it has been taking data since September 2018. The experimental detection technique used in both DUNE and ProtoDUNE-SP experiments is the Liquid Argon Time Projection Chamber (LArTPC). The study of the present work focused on estimating the Rayleigh scattering length in the ProtoDUNE-SP experiment. The analysis of the data indicates a Rayleigh scattering length of approximately 97^{+25}_{-15} cm, which coincides with the analytically estimated value.

Keywords: Neutrinos; Scintillation counters; Liquid argon.

List of Figures

2.1.1	Scheme of the locations of the near and far detectors for the DUNE experiment. The near detector is going to be located at Fermilab, and the far detector is going to be located in the Sanford Underground Research Facility in South Dakota [11].	31
2.1.2	Underground caverns for DUNE's far detectors at SURF, in South Dakota [11].	31
2.1.3	The single-phase (left) and the dual-phase (right) readout designs [15, 14].	32
2.2.1	Particle event registered by the experiment MicroBooNE, that also uses the LArTPC technology [17].	33
3.0.1	Left: Emission spectrum of liquid argon at 85 K (black line) and gaseous argon at 295 K (red line) [19]. Right: The emission spectra of both slow and fast components [20].	36
3.1.1	Electron attachment rate constant in liquid argon for different contamination types [21].	38
3.1.2	Example of waveforms for 0 ppm, 0.6 ppm and 2 ppm oxygen contamination [22]. It is possible to notice that all three scintillation fast-component lifetimes coincide, and there is less scintillation slow-component light as contamination increases.	39
3.1.3	Slow scintillation light component for different oxygen contamination concentrations for the WArP 2.3 L prototype (left) and the small 0.7 L dedicated detector (right) [22].	40
3.1.4	Emission spectra of argon (black), and absorption spectra of argon (red). The peaks have been normalized to show the same intensity at the maximum [25, 26, 27].	41

4.1.1 Left: The major components of the ProtoDUNE-SP TPC. Right: View of the ProtoDUNE-SP wire plane arrangement with two induction layers (green and magenta, $\pm 35.7^\circ$ w.r.t. the vertical) and one collection plane (blue, $\pm 0^\circ$ w.r.t. the vertical) [28].	43
4.2.1 Dichroic filter transmission (left) and reflection (right) [30].	45
4.2.2 ARAPUCA array in ProtoDUNE-SP [13].	46
4.2.3 Schematic of scintillation light detection with dip-coated light guide bars (Ref. [13]).	46
4.2.4 Schematic of the double-shift light guide concept [13].	47
4.4.1 An example of the smoothing process, in which it is possible to see the raw data (black line) and the smoothed one (red line), using the combination of the moving average and the total variation denoising algorithm.	49
4.4.2 Histogram of the integral of the signal for channel 264. The first peak centered in zero represents the integral of empty waveforms, in other words, it is the baseline peak. The consecutive equally-spaced peaks represent the integrals of the multiple integers of photoelectrons (p.e.).	50
5.1.1 Cosmic Run Tagger design for ProtoDUNE-SP. The position of the modules allows identifying events from cosmic rays parallel to the beam [28].	53
5.1.2 Scheme of the photon detection system for data collection after an external trigger.	53
5.2.1 Charge spectrum histograms for internal trigger data in cosmic runs. The distributions for channels 100, 104, 132, 108 and 112 are displayed. The difference in the number of entries of each run is due to the fact that they do not have the same duration and, therefore, they have not collected the same amount of data.	55
5.2.2 Charge spectrum histogram for internal trigger data in cosmic runs, using different thresholds for run 4573 and channel 132.	56
5.2.3 Electron lifetime and oxygen concentration in ProtoDUNE-SP from September, 2018, to January, 2019. The oxygen concentration was calculated using Equation 3.1.3 and the constant rate for oxygen at 500 V/cm. The electron lifetime was measured using three purity monitors from the ICARUS T600 detector [35] installed at the top (red), middle (black) and bottom (blue) of the TPC. Note that the concentration varies over time making it crucial to understand if light is affected by this variation.	56

5.2.4 LAr scintillation light waveform caused by the passage of an alpha (green) and muon (red) particles into liquid argon [36].	57
5.2.5 Vertical flux of cosmic rays at different altitudes [7].	58
5.2.6 (Left) Waveforms for three different configurations: LAr scintillation light (red), LAr+TPB scintillation light (blue) and LAr+TPB scintillation light convoluted with the normalized Gaussian (black). (Right) Example of how the convolution is calculated. The convolution result is the sum of all the contributions from the Gaussian before that point. The amplitude of all three curves are normalized to be equal to 1 in both plots.	60
6.1.1 Example of an undershoot. The undershoot effect shown in this figure is exaggerated from that observed in the experimental data of the ProtoDUNE-SP experiment.	62
6.1.2 Average waveform for a double-shifted light guide. DAQ channels 252 and 253. . .	63
6.1.3 Average waveform for a dip-coated light guide. DAQ channels 257 and 258.	64
6.1.4 Average waveform for an ARAPUCA with 6 SiPMs installed in each. DAQ channels 264 and 265.	64
6.1.5 Average waveform for an ARAPUCA with 12 SiPMs installed in each. DAQ channels 268 and 269.	65
6.1.6 Fit (red) done on the average waveform (blue) of channel 269 in run 4588.	66
6.1.7 The LAr scintillation light slow decay time component for some channels in APA 6 of the ProtoDUNE-SP experiment. Channels 252 and 253 are Double-Shifted light guide bars. Channels 257 and 258 are Dip-Coated light guide bars. Channels 264 and 265 (268 and 269) are ARAPUCAs with six (12) SiPMs installed in each.. . .	66
6.2.1 Beam momentum distribution for beam runs 4878 and 5837.	67
6.2.2 Average waveforms for a 0.5 GeV beam signal for run 4878 (blue) and run 5837 (red). The average waveform was calculated considering only the pulses of light generated by the beam of particles, disregarding those generated by cosmic rays. .	68
6.2.3 Total number of photons detected by 12 ARAPUCA channels together for a particle beam of 0.5 GeV. The particle identification was done using both time-of-flight and Cerenkov detector information.	69

6.2.4	Fit of two Gaussians on the integral histogram distribution. The peak near zero represents the resulting integrals of empty waveforms, and the second peak represents the resulting integrals of waveforms associated to the beam.	70
6.2.5	Number of photons detected by channel 134 for a particle beam of 0.5 GeV.	70
6.3.1	Stopping power of electrons in liquid argon [40].	71
6.3.2	LET dependence of scintillation yield, Y, in liquid argon. Solid circles show the yields for relativistic particles. Non-relativistic particles are represented by open circles. Open squares and triangles show the yield for non-relativistic protons whereas small open circles show those for non relativistic-helium ions [41].	72
6.3.3	Saturation curves of ionization (open symbols) and scintillation (close symbols) for 1 MeV electrons in LAr (dots) and in liquid Xenon (squares) as function of the electric field strength [41].	73
6.3.4	Number of simulated photons detected by the ARAPUCA module for different Rayleigh scattering lengths. The smaller the Rayleigh scattering length, the smaller is the quantity of photons arriving at the detector due to the greater probability of absorption along the track. From the interception of the band of detected photons given by the simulation (red) and the band of measured detected photons for run 5837 given by Figure 6.2.4 (gray), it was possible to measure a Rayleigh scattering length of 97^{+25}_{-15} cm.	75
6.3.5	Distance travelled by the photon until its detection by the ARAPUCA module for different Rayleigh scattering lengths.	75
6.3.6	Number of detected photons for different absorption lengths, for a fixed Rayleigh scattering length of 97 cm. From the interception of the band of detected photons given by the simulation (red) and the band of measured detected photons for run 4878 given by Figure 6.2.4 (gray), it was possible to measure an absorption length of 2415^{+2639}_{-897} cm.	76

List of Tables

1.1	Proton and neutron information (Ref. [7]).	28
2.1	Noble liquid elements properties.	34
3.1	Properties and relevant information of the liquid argon scintillation light.	38
4.1	APA identification system according to the DAQ channels. The particle beam enters the TPC on the left side of APA 3, which means that APA 4, APA 5 and APA 6 cannot see the beam signals due to the presence of the cathode dividing the two TPCs. Note that RaS(DaS) stands for Rack Side(DAQ Side) of the TPC.	44
4.2	Information about the optical properties of each light detection device installed in the ProtoDUNE-SP experiment. Hamamatsu (HMM) and Sense Light (SensL) SiPMs were used.	47
4.3	Calibration for the ARAPUCA channels on the APA 3. The calibration is given in ADC×ticks and the calibration with correction takes into account crosstalks.	51
5.1	Information on the runs used for the energy spectra shown in Figure 5.2.1.	54
5.2	Selected beam run information. The electron lifetime was measured using the monitor 1, that is close to the ARAPUCA array in APA 3. For both cases, the TPC cathode voltage was 180 kV and the ARAPUCA bias voltage was 48 V.	60
6.1	Run selection for the analysis of the average waveform. Those runs were selected due to their oxygen concentration.	61
6.2	Selection of the channels for the analysis of the slow scintillation component of liquid argon.	62
6.3	Summary of important information used in the Monte Carlo toy model described in this section.	76

List of Abbreviations

APA: Anode Plane Assembly

ARAPUCA: Argon R&D Advanced Program at UniCamp

CP: Charge Parity

CPA: Cathode Plane Assembly

CRT: Cosmic Run Tagger

DaS: DAQ Side

DCM: DUNE Calibration Module

DUNE: Deep Underground Neutrino Experiment

DP: Dual-Phase

Fermilab: Fermi National Accelerator Laboratory

GAr: Gaseous Argon

LAr: Liquid Argon

LArTPC: Liquid Argon Time Projection Chamber

LBNE: Long Baseline Neutrino Experiment

LET: Linear Energy Transfer

LNGS: Gran Sasso INFN Laboratory

NP: Neutrino Platform

PDS: Photon Detection System

PTP: P-terphenyl

RaS: Rack Side

R&D: Research and Development

SiPM: Silicon Photomultiplier

SP: Single-Phase

SSP: SiPM Signal Processor

LIST OF ABBREVIATIONS

SURF: Sanford Underground Research Facility

TPB: Tetraphenyl Butadiene

TPC: Time Projection Chamber

VUV: Vacuum Ultra Violet

WArP: Wimp Argon Programme

Contents

Acknowledgements

Resumo

Abstract

List of Figures

List of Tables

List of Abbreviations

Contents

Introduction	19
1 Introduction to the DUNE's Physics Goals	22
1.1 The neutrino postulate	22
1.2 Matter-antimatter asymmetry	24
1.3 CP violation	25
1.4 Proton decay	27
1.5 Neutrino from supernovae	28
2 The DUNE experiment	30
2.1 Introduction	30
2.2 Liquid Argon Time Projection Chamber	33
3 Scintillation light in LAr	35
3.1 Effects of contamination in liquid argon scintillation	37

3.1.1	Quenching	37
3.1.2	WArP oxygen contamination test	38
3.1.3	Rayleigh scattering and absorption	40
4	The ProtoDUNE-SP experiment	42
4.1	Charge detection system in ProtoDUNE-SP	42
4.2	Photon detection system in ProtoDUNE-SP	43
4.2.1	ARAPUCA	44
4.2.2	Dip-coated light guides	46
4.2.3	Double-shift light guides	46
4.3	Silicon photomultiplier	47
4.4	Calibration	48
5	Data Selection	52
5.1	Data acquisition	52
5.2	Internal Trigger	53
5.2.1	Data sample for internal trigger	55
5.2.2	Cosmic rays at sea level	58
5.2.3	Signal modelling	59
5.3	Beam external trigger	60
6	Signal Analysis	61
6.1	Quenching analysis	61
6.1.1	Average Waveform	61
6.1.2	Slow decay time measurement	65
6.2	Rayleigh scattering analysis	66
6.3	Monte Carlo toy model	71
7	Conclusions	77
	Bibliography	80

Introduction

Neutrinos have always intrigued scientists since they were postulated. At that time, beta decay measurements did not seem to preserve energy, since the energy of the daughter nucleus and the emitted electron did not sum up the total initial energy. In 1930, Wolfgang Pauli proposed the existence of a massless and neutral particle that would also be emitted during the beta decay and would carry the missing energy. This particle, so called *neutrino*, was first detected in 1956 and it was responsible for the beginning of a whole new field of studies in Physics.

Currently, many experiments are built to study neutrinos. The present work has been carried out in the context of the DUNE (Deep Underground Neutrino Experiment) experiment (Chapter 2), which is one of the most important experiments in the field of neutrino physics. DUNE is a long-baseline experiment with the near detector located at Fermilab and the far detector located 1,300 km away at the Sanford Underground Research Facility in South Dakota (US). DUNE is a project for the construction of the biggest Liquid Argon Time Projection Chamber ever built, with an active volume of 40 kton, for the study of some of the open questions about neutrinos (Chapter 1), the eventual detection of neutrinos emitted in a Supernova explosion in our Galaxy, and of proton decay.

DUNE uses the experimental detection technique called Liquid Argon Time Projection Chamber (LArTPC), started by ICARUS Collaboration in the 80s and substantially improved in the last ten years thanks to an extended Research and Development program carried out by several international collaborations. The operation of this technology relies on the formation and detection of free electrons and scintillation light (Chapter 3), induced by the passage of an ionizing particle in the active volume. Scintillation light is commonly used to determine the time t_0 in which an interaction happened, and this information allows the complete three-dimensional reconstruction of the event. Moreover, particle identification

can be done using a combination of signals coming from scintillation light and free electrons, which is crucial to study neutrino oscillations. Studies have been carried out to determine the possibility of using light to do calorimetry, which would increase the energy resolution of the detector.

The proper operation of the LArTPC technology depends on the purity of the liquid argon. In particular, light might undergo changes due to the presence of impurities in the active volume of liquid argon. The first possible effect is quenching (Section 3.1.1) and it consists of a two-body collision between the impurities and excited argon molecules that affects the shape of the light pulse. A second effect is absorption that, in addition to Rayleigh scattering (Section 3.1.3), decreases the number of photons that reach the light detector.

The shape and the intensity of the light signal can thus be significantly deteriorated by the presence of impurities in liquid argon. Although liquid argon produces a great amount of light per energy deposited, the size of the LArTPC, the wavelength of the scintillation light, and the light scattering in argon itself will decrease the number of detected photons. For instance, it will be hard to detect and to reconstruct events of supernova neutrinos since they produce low energy particles that are not beam-triggered. A complete understanding of the relationship between the level of impurities and the light propagation in the active volume may increase the accuracy of event reconstructions and the optimization of the simulation. The comprehension of this relation may also contribute to the optimization of light detection, allowing to establish the detector configuration, efficiency and event threshold.

DUNE launched a major scientific and technological challenge. Studies are nowadays focused on the optimization of light detection by the reasons listed above, as well as trying to improve the performance of the detectors in particle tracking from free electrons. For this reason, all technologies that are intended to be installed in DUNE are currently being tested in the ProtoDUNE-SP experiment (Chapter 4), which is the large-scale prototype of DUNE, with a total mass of 770 ton of liquid argon. It is installed at CERN and is taking data since September 2018. The largest LArTPCs ever built are the ones of ProtoDUNE-SP (770 ton of liquid argon) and ICARUS (600 ton of liquid argon) experiments which, despite their size and success, are both much smaller than the proposed chamber for DUNE.

In the present work, a study of the behavior of the detected light as a function of the purity level of liquid argon in ProtoDUNE-SP was made. Above all, a study of the Rayleigh scattering

was made in order to obtain the scattering length of the light which has direct implications on the amount of detected light. For such a study, a set of runs from the beginning of data taking of the ProtoDUNE-SP experiment (Chapter 5) were chosen to be analyzed (Chapter 6), because they have the highest level of contamination of the whole period of data taking.

To study quenching, a signal model based on studies of liquid argon scintillation light in combination with the detector response was assumed and compared to the measured self-triggered pulses of light. To study absorption and Rayleigh scattering, a Monte Carlo simulation (Section 3.1.3) was developed to estimate the Rayleigh scattering length necessary to recover the number of detected photons for beam data for two different impurity concentrations.

Although liquid argon has been used in experiments designed to detect ionizing particles, there are several open questions regarding the detector performance. One of these questions regards Rayleigh scattering since event reconstruction depends on the location of the event. For such, the light scattering presents a potential design constraint. The attenuation of the light can be caused by the absorption of light by impurities and Rayleigh scattering. An increase in the amount of detected light is expected for large scattering lengths. However, for smaller lengths, a decrease in the amount of light is expected, and higher detection efficiency would be necessary.

Chapter 1

Introduction to the DUNE's Physics Goals

1.1. The neutrino postulate

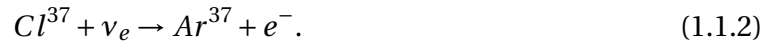
In the early 20th century, the observation of the beta decay led to questioning about one of the main laws of physics: the energy conservation law. Originally, the beta decay was thought to be the decay of a nucleus into a lighter nucleus with the emission of an electron. In the center of mass of the decaying nucleus, the electron energy can be written as

$$E = \left(\frac{m_1^2 - m_2^2 + m_e^2}{2m_1} \right) c^2 \quad (1.1.1)$$

where E is the electron energy, m_1 is the mass of the decaying particle, m_2 is the mass of the daughter and m_e the mass of the electron. Therefore, the energy of the emitted electron should be constant. However, James Chadwick, while studying the beta decay, measured a continuous energy distribution for the electron, which apparently violates the conservation of energy, one of the strongest laws in physics. To save this law, in 1930, Wolfgang Pauli proposed the existence of a massless and neutral particle that would also be emitted during the beta decay and would carry the missing energy. Enrico Fermi was the first one to call this particle *neutrino*. In 1956, the Cowan-Reines neutrino experiment measured the first neutrinos from a beta decay, proving Pauli's prediction. This discovery resulted in the Nobel Prize in 1995 for Frederick Reines.

In 1960, John Bahcall, using the Standard Solar Model [1, 2], made the first calculation of the expected neutrino flux coming from the Sun, and in 1968, alongside with the astrophysicist Raymond Davis, John Bahcall headed the Homestake experiment [3] in South Dakota to try to confirm his predictions. The idea was to measure the solar electron neutrinos each

captured by a chlorine-37 nucleus and resulting in an argon atom plus an electron,



Therefore, by counting the number of argon atoms formed, it would be possible to determine the number of captured neutrinos. This experiment was the first one to successfully detect and count solar neutrinos. Unfortunately, the number of detected solar neutrinos was around 1/3 of the predicted. The discrepancy between the observed fluxes and the calculations is known as *the solar neutrino problem*.

This discrepancy could be explained by one of the Pontecorvo's [4] hypothesis that neutrinos could oscillate in flavor¹. This oscillation means that the electron neutrino produced in the core of the Sun could change its flavor during its way to Earth, decreasing the electron neutrino flux and increasing the fluxes of neutrinos of other flavors. The Sudbury Neutrino Observatory (SNO) experiment (1984) was an attempt to provide a definitive answer to the solar neutrino problem. This experiment used a chamber of heavy water containing deuterium (D₂O) which allowed the measurement of two separate reactions on deuteron (*d*): a charged current (CC) reaction that was sensitive only to electron neutrinos,



and a neutral current (NC) reaction that was equally sensitive to all neutrino types,



Finally, neutrino flux measurements were in agreement with the calculations. The total flux of all neutrino flavors measured by the SNO experiment agreed with the theoretical prediction made by Bahcall.

The confirmation of the neutrino flavor oscillations led to a new neutrino physics era. Many experiments started to study neutrinos more closely, exploring different energy ranges, decay channels and neutrinos sources. A few recent experiments are:

- Neutrinos from accelerators: MiniBooNE (2002), MINOS (2005), OPERA (2008), MINERvA (2009), ICARUS (2010), NOvA (2011), MicroBooNE (2014), DUNE (future);
- Neutrinos from nuclear reactors: Daya Bay (2011), and Double Chooz (2011);

¹There are three neutrino flavors: electron neutrino (ν_e), muon neutrino (ν_μ), and tau neutrino (ν_τ).

- Neutrinos from outer space: Kamiokande (1986), LVD (2005), IceCube (2006), Borecino (2007), JUNO (2014).

This dissertation is embedded in the context of the Deep Underground Neutrino Experiment (DUNE) (see chapter 2). This experiment is part of the Long Baseline Neutrino Experiment (LBNE) in the United States. The far detector is going to be the biggest liquid argon detector ever built, with a total volume of 40-kton of liquid argon located at the Sanford Underground Research Facility (SURF). The primary science goals include measurements of the charge parity (CP) phase, determination of the neutrino mass ordering, measurement of the mixing angle θ_{23} , determination of the octant in which this angle lies, studies of supernovae neutrinos, and search for a proton decay. Answering these questions could lead us to complete the missing information to confirm or not the big bang theory.

1.2. Matter-antimatter asymmetry

The big bang theory is a model that describes the development of the universe from the beginning. This model offers a satisfactory explanation for experimental observations such as the composition of the universe, the existence of the cosmic microwave background, the average temperature of $\sim 2.8\text{K}$ and its expansion. The missing piece of the puzzle is that all of these arguments presuppose the existence of an equal amount of matter and antimatter at the beginning of the universe. But experimental evidence shows that we live in a matter-dominated universe, and no experimental observation shows any concentration of antimatter in the observable universe. Therefore, something might have generated this asymmetry between matter and antimatter, which is known as *baryogenesis*.

In 1967, Andrei Sakharov proposed three necessary conditions, known as *Sakharov conditions*, to explain the different rate between matter and antimatter in the universe:

1. Interactions out of thermal equilibrium,
2. CP violation, and
3. Baryon number violation.

Since then, particle physics experiments have been trying to measure these variables. In particular, the physics goals of the DUNE include measurements that could contribute to

the ascertainment of at least two of the Sakharov conditions:

1. CP violation: by measuring the δ_{CP} phase and
2. Baryon number violation: by trying to measure the proton decay.

The next two sections provide a brief context of the physics that DUNE will study, and therefore, a complete derivation is not provided.

1.3. CP violation

In the standard theory of neutrino oscillations [5, 6, 7] a neutrino with flavor l created in a charged-current weak interaction process from a charged lepton, is described by the flavor state

$$|\nu_l\rangle = \sum_j^3 U_{lj}^* |\nu_j\rangle \quad l = e, \mu, \tau \quad (1.3.1)$$

that can be written in matrix form as

$$\begin{pmatrix} \nu_e \\ \nu_\mu \\ \nu_\tau \end{pmatrix} = \begin{pmatrix} U_{e1} & U_{e2} & U_{e3} \\ U_{\mu1} & U_{\mu2} & U_{\mu3} \\ U_{\tau1} & U_{\tau2} & U_{\tau3} \end{pmatrix} \begin{pmatrix} \nu_1 \\ \nu_2 \\ \nu_3 \end{pmatrix} \quad (1.3.2)$$

where $|\nu_l\rangle$ are the flavor states, $|\nu_j\rangle$ are the mass states and U_{lj} is the mixing matrix, also known as Pontecorvo-Maki-Nakagawa-Sakata (PMNS) matrix, defined as

$$U = \begin{pmatrix} c_{12}c_{13} & s_{12}c_{13} & s_{13}e^{-i\delta_{CP}} \\ -s_{12}c_{23} - c_{12}s_{23}s_{13}e^{i\delta_{CP}} & c_{12}c_{23} - s_{12}s_{23}s_{13}e^{i\delta_{CP}} & s_{23}c_{13} \\ s_{12}s_{23} - c_{12}c_{23}s_{13}e^{i\delta_{CP}} & -c_{12}s_{23} - s_{12}c_{23}s_{13}e^{i\delta_{CP}} & c_{23}c_{13} \end{pmatrix} \begin{pmatrix} e^{i\alpha} & 0 & 0 \\ 0 & e^{i\beta} & 0 \\ 0 & 0 & 1 \end{pmatrix}, \quad (1.3.3)$$

where $s_{ij} = \sin\theta_{ij}$, $c_{ij} = \cos\theta_{ij}$, θ_{ij} are the mixing angles, and δ_{CP} is the CP complex phase. Here, α and β are the so-called Majorana phases that are decoupled from the phenomenon of neutrino oscillation. This unitary matrix contains information about the mismatch of quantum states of neutrinos when they propagate through matter.

Usually, experiments that aim to study neutrino oscillation consist of a long baseline with a near and a far detector. The near detector, usually a few hundred meters away from

the neutrino source, measures the initial neutrino flux. The far detector, whose distance depends on the energy to be studied², measures the final flux of neutrinos. Therefore, by measuring the difference between the initial and the final fluxes, one can calculate the probability of oscillation between two flavor eigenstates, $\nu_l \rightarrow \nu_{l'}$.

As mentioned before, a neutrino can be described as a quantum state composed of a superposition of mass eigenstates with a wavefunction $|\Psi(0)\rangle$ at the time $t = 0$ of

$$|\Psi(0)\rangle = |\nu_l(0)\rangle \equiv \sum_{i=1}^3 U_{li}^* |\nu_i\rangle, \quad (1.3.4)$$

and its time evolution corresponds to

$$|\nu_l(t)\rangle = e^{-iHt} |\nu_l(0)\rangle. \quad (1.3.5)$$

Since $|\nu_l\rangle$ is not an eigenstate of the Hamiltonian, it is easier to calculate the time evolution using the mass eigenstates since $|\nu_i\rangle$ is eigenstate of the Hamiltonian, and $H|\nu_i\rangle = E_i |\nu_i\rangle$.

Using the mass eigenstates, Equation 1.3.5 becomes

$$|\nu_l(t)\rangle = \sum_{i=1}^3 e^{-iHt} U_{li}^* |\nu_i\rangle = \sum_{i=1}^3 e^{-iE_i t} U_{li}^* |\nu_i\rangle, \quad (1.3.6)$$

that can be written in terms of the flavor states as

$$|\nu_l(t)\rangle = \sum_{\beta=1}^3 \sum_{i=1}^3 e^{-iE_i t} U_{\beta i} U_{li}^* |\nu_{\beta}\rangle, \quad (1.3.7)$$

where β sums over the flavor states. So, starting from state $|\nu_l\rangle$, the probability of observing a neutrino flavor state $|\nu_{\beta}\rangle$ after time t is given by

$$\begin{aligned} P(\nu_l \rightarrow \nu_{\beta}) &= |\langle \nu_{\beta} | \nu_l(t) \rangle|^2 \\ &= \left| \sum_{i=1}^3 e^{-iE_i t} U_{\beta i} U_{li}^* \right|^2 \\ &= \sum_{i=1}^3 \sum_{j=1}^3 U_{li}^* U_{lj} U_{\beta i} U_{\beta j}^* e^{-i(E_i - E_j)t}. \end{aligned} \quad (1.3.8)$$

The relativistic energy of neutrinos can be written as $E = p + (m^2/2p)$ considering their small mass and high momentum. Since all neutrino mass states i are produced coherently,

²As shown in the Eq.1.3.10, the oscillation probability depends on L/E , where L is the distance between the near and the far detector and E is the neutrino energy.

their momenta p are the same, and because neutrinos are relativistic, their energy can be written as $E = pc = pL/t$, and Equation 1.3.8 can be written as

$$P(\nu_l \rightarrow \nu_\beta) = \sum_{i=1}^3 \sum_{j=1}^3 U_{li}^* U_{lj} U_{\beta i} U_{\beta j}^* e^{-i \frac{L}{2E} \Delta m_{ij}^2}, \quad (1.3.9)$$

where $\Delta m_{ij}^2 = m_i^2 - m_j^2$ ($m_{i,j}$ are the masses of the mass eigenstates). Another way to write this equation is:

$$\begin{aligned} P_{\pm} = & \delta_{l\beta} - 4 \sum_{i>j} \text{Re} \left(U_{\beta i} U_{\beta j}^* U_{li}^* U_{lj} \right) \sin^2 \left(\frac{\Delta m_{ij}^2 L}{4E} \right) \\ & \pm 2 \sum_{i>j} \text{Im} \left(U_{\beta i} U_{\beta j}^* U_{li}^* U_{lj} \right) \sin^2 \left(\frac{\Delta m_{ij}^2 L}{2E} \right) \end{aligned} \quad (1.3.10)$$

where E is the neutrino energy, L is the distance traveled by the neutrino, $P_- = P(\bar{\nu}_l \rightarrow \bar{\nu}_\beta)$ and $P_+ = P(\nu_l \rightarrow \nu_\beta)$ are the oscillation probabilities for antineutrinos and neutrinos respectively. The CP violation can be understood as the measurement of how different particles and antiparticles are, and one way to do this measurement is to see the difference of the oscillation probabilities between neutrinos and antineutrinos [8], given by

$$\Delta P \equiv P(\nu_l \rightarrow \nu_\beta) - P(\bar{\nu}_l \rightarrow \bar{\nu}_\beta) = -16 J_{l\beta} \sin \Delta_{12} \sin \Delta_{23} \sin \Delta_{31}, \quad (1.3.11)$$

where $\Delta_{ij} \equiv \Delta m_{ij}^2 L / 4E$ and

$$J_{l\beta} \equiv \text{Im} \left(U_{l1} U_{l2}^* U_{\beta 2}^* U_{\beta 1} \right) = \pm J, \quad J \equiv s_{12} c_{12} s_{23} c_{23} s_{13} c_{13}^2 \sin \delta_{CP}, \quad (1.3.12)$$

which makes it explicit how the measurement of δ_{CP} can provide information about the relation between matter and antimatter since $\Delta P \propto \sin \delta_{CP}$.

Another important point to highlight is that the oscillation probability, Equation 1.3.10, depends on the difference of squared masses of the initial and the final flavor eigenstates, $\Delta m_{\text{initial,final}}^2$. Therefore, it is not possible to measure the absolute mass by measuring neutrino oscillations.

1.4. Proton decay

An effective way to study baryonic number violation is through the proton decay [9]. Baryons are those particles made by three quarks. The most famous baryons are *protons* and

neutrons, see Table 1.1. The baryon decay occurs frequently in nature. An example of baryon decay is the beta decay shown below

$$n \rightarrow p + e^{-} + \bar{\nu}_e \quad (1.4.1)$$

that satisfies baryonic number and energy conservation. Since the proton is the lightest baryon, it can not decay into another baryon while conserving both energy and baryonic number. Therefore, an observation of proton decay would mean an evidence of baryonic number violation.

Table 1.1: Proton and neutron information (Ref. [7]).

Particle Name	Composition	Rest Mass (MeV/c ²)
Proton	uud	938.272081 ± 0.000006
Neutron	udd	939.565413 ± 0.000006

The lowest limit of proton lifetime of 10^{34} years was measured by the Super-Kamiokande experiment during 10 years of data acquisition. In other words, it means that none of the 7.5×10^{33} protons present in the experiment's fiducial volume decayed during the data taking. The proton lifetime is extremely long when compared to the age of the universe, which is estimated to be approximately 138×10^8 years.

In addition, the Standard Model of Particle Physics predicts the conservation of the baryonic number. Thus, the observation of proton decay would be an evidence of physics beyond the Standard Model.

1.5. Neutrino from supernovae

In the context of cosmology, DUNE proposes to study neutrinos stemming from the collapse of supernovae. Stars form because a large enough cloud of particles is unstable under gravity. The cloud contracts and more than 99% of its gravitational binding energy is released as neutrinos. The most important processes in supernova and proton neutron star matter are described in [10]. During the explosion, more neutrinos are produced than the number released in the rest of the star's life combined. Experiments are constantly looking for this sudden increase in the number of neutrinos, which might indicate the occurrence of a supernova. In particular, the improvement of the light detection system, such as the ARAPUCA

device (see Section [4.2.1](#)) seeks to provide better conditions for the detection of the signal generated by these neutrinos, typically in the few to few tens of MeV regime.

Chapter 2

The DUNE experiment

2.1. Introduction

DUNE [11] is an international project hosted by the Fermi National Accelerator Laboratory (Fermilab) and will be part of the LBNE at this laboratory. DUNE aims to provide information for our understanding of the universe by studying neutrinos, one of the most mysterious elementary particles we know. The physics goals of the DUNE experiments are as following:

1. Use ν_μ and $\bar{\nu}_\mu$ beams from Fermilab to study neutrino oscillations. This program includes measurements of the CP phase, determinations of the neutrino mass ordering (the sign of $\Delta m_{31}^2 \equiv m_3^1 - m_2^1$), measurement of the missing angle δ_{23} and the determination of the octant in which this angle lies, and the test of the three-neutrino paradigm¹.
2. Search for proton decay in several important decay modes. The observation of proton decay would represent a ground-breaking discovery in physics, providing a key requirement for grand unification of the forces.
3. Detect and measure the ν_e flux from a core-collapse supernova within our galaxy. Such a measurement would provide a wealth of unique information about the early stages of the core-collapse, and could even indicate the birth of a black hole.

¹Not all of the neutrino data are successfully described by the standard three-neutrino paradigm. However, there are hints, coming from a variety of sources, that nature may contain more than three neutrino mass eigenstates [12].

Neutrinos are the second most abundant particle in the universe, $\sim 300 \nu/\text{cm}^3$. Despite their abundance, since their cross section is small, it is difficult to detect them. For this reason, large detectors and an intense neutrino flux are needed in order to increase the interaction probability. DUNE will satisfy both these conditions.

The experiment will consist of two detectors. The near one will be located at Fermilab, 575 m away from the neutrino source, and will be responsible for measuring the intensity and the energy spectrum of the beam. The far detector will be located at SURF in South Dakota and will be 1.5 km underground and 1,300 km (800 miles) away from Fermilab, Figure 2.1.1.

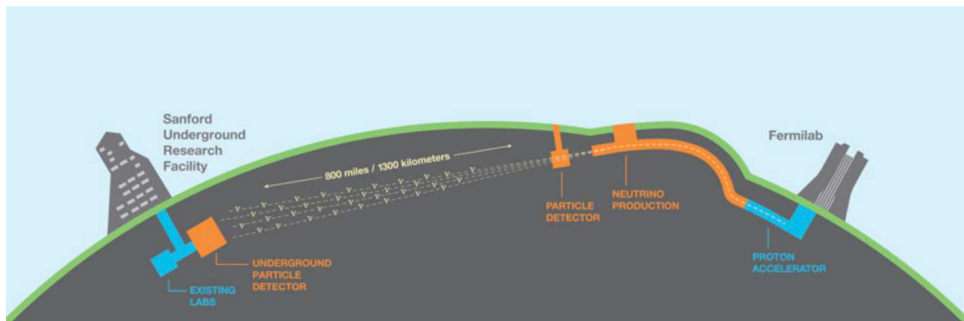


Figure 2.1.1: Scheme of the locations of the near and far detectors for the DUNE experiment. The near detector is going to be located at Fermilab, and the far detector is going to be located in the Sanford Underground Research Facility in South Dakota [11].

The far detector is going to be a very large, modular Liquid Argon Time Projection Chamber (LArTPC), see Section 2.2, with a 40 kton fiducial mass. Each one of the four modules, Figure 2.1.2, will be 14 m (width) \times 14.1 m (height) \times 62.0 m (length). Fermilab will shoot the most intense ν_μ and $\bar{\nu}_\mu$ beam in the world to study neutrino oscillations, with a 80 GeV primary proton beam and a beam power up to 1.2 MW.

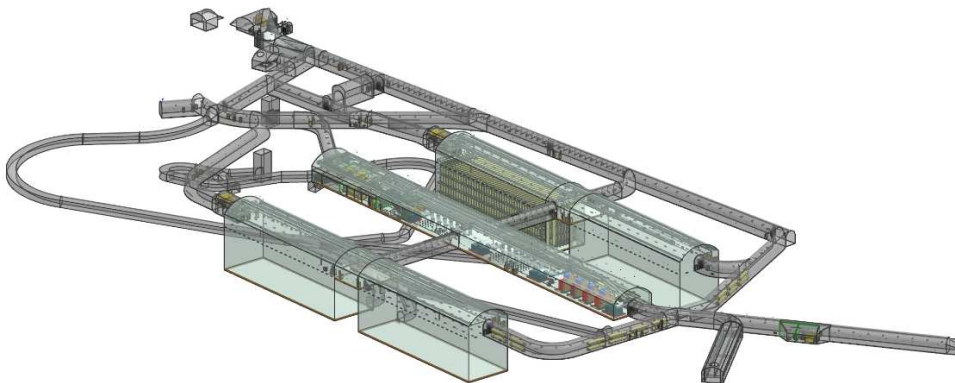


Figure 2.1.2: Underground caverns for DUNE's far detectors at SURF, in South Dakota [11].

DUNE is planning on having two kinds of LArTPCs:

- The **single-phase** (SP) [13] is a chamber filled with pure liquid argon. This technology was started by the ICARUS Collaboration in the 1980s and was substantially improved in the last ten years thanks to an extended Research and Development (R&D) program carried out by several international collaborations (MicroBooNE, SBND, LArIAT, ...). The charge produced by the passage of an ionizing particle is drifted horizontally through a homogeneous liquid argon medium until its capture by a wire plane.
- The **dual-phase** (DP) [14] is going to be a chamber filled with liquid and gaseous argon. Due to matter density, gaseous argon occupies the top half of the chamber, and liquid argon the bottom one. The Large Electron Multiplier dividing the gaseous and the liquid mediums, see Figure 2.1.3 (left), will cause a signal amplification that will allow the ability to search for neutrinos signatures in a new way. This technology is not yet as well studied as the SP one.

An example of the pattern captured by the wire planes in the SP is given in Figure 2.1.3 (left) and the DP detection process is outlined in Figure 2.1.3 (right). Both systems are going to collect electrons and scintillation light. While the SP drifts the electrons horizontally, the DP drifts them vertically.

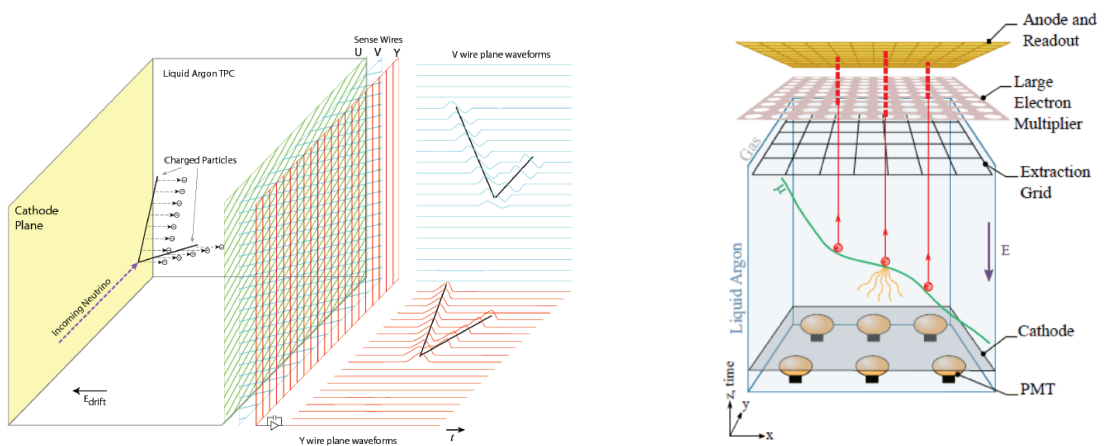


Figure 2.1.3: The single-phase (left) and the dual-phase (right) readout designs [15, 14].

The LArTPC technology was chosen because it allows researchers to record in detail the particles originating in the collision of neutrinos and atoms of the detector. Many exper-

iments have proven the excellent spatial and calorimetric resolution of this technology. It also provides high quality tracking of charged particles trajectories down to low momenta.

2.2. Liquid Argon Time Projection Chamber

First proposed by Carlo Rubbia in 1977 [16], a LArTPC aimed to be a novel neutrino detector that combines the high resolution of bubble chambers with the massive target characteristic of electron detectors. Currently, they are one of the most advanced experimental technologies for physics at the Intensity Frontiers due to their full three-dimensional imaging, excellent particle identification and precise calorimetric energy resolution. The signature of an event recorded in the MicroBooNE experiment, that also uses the LArTPC technology, is shown in Figure 2.2.1. For the purpose of this dissertation, the author is going to focus on the LArTPC-SP because the data analysis exposed in this work is from the ProtoDUNE-SP data, see Chapters 4 and 5. ProtoDUNE-SP is an experiment installed at CERN to ensure that all parts of the technology are well studied and tested.

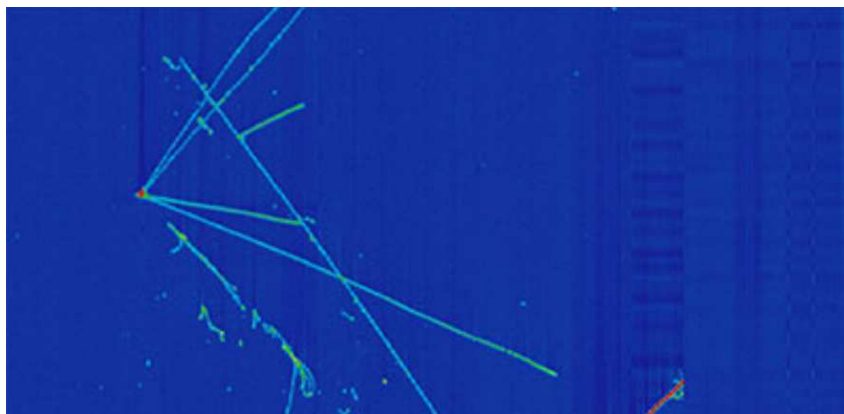


Figure 2.2.1: Particle event registered by the experiment MicroBooNE, that also uses the LArTPC technology [17].

The LArTPC technology is the structure that allows reconstructing a three-dimensional image of interactions that happen inside the detector. This structure is placed inside a cryostat that maintains the low temperature of 89 K for the argon in the liquid phase stable. Therefore the LArTPC is filled and surrounded by LAr and, for a matter of definition, the volume of LAr inside the detector is called *active volume*. The passage of an ionizing particle is going to produce ionization and scintillation light along the track.

The basic idea of this technology is to drift the free electrons from an ionizing track towards one wall using a uniform electric field. The charge collection system is made of several wires placed in different parallel planes, oriented in such a way that the combination of their signals allows locating at which point of the plane the electron has been detected.

The scintillation light is used to extract the third spacial component of the interaction. Since the speed of light in liquid argon is much faster than the drift velocity of the electrons², light is usually used to determine the time t_0 when the interaction happened. By knowing the time difference between detection of the light and the charge signals, and the drift velocity of the electrons, it is possible to calculate the distance traveled by the electron perpendicular to the wire plane. In other words, it is possible to recover the missing spatial component for the total three-dimensional reconstruction of the interaction.

The choice of the active volume material of the detector deserves special attention. Noble elements are widely used as active volume since their valence shell is complete, which allows long electron drifts inside the detector. The elements most commonly used as active volume of particle detectors are helium, neon, argon, krypton, xenon and water. The properties of these elements are displayed in Table 2.1.

Table 2.1: Noble liquid elements properties.

	He	Ne	Ar	Kr	Xe	Water
Boiling Point [K] @ 1 atm	4.2	27.1	87.3	120.0	165.0	373
Density [g/cm ³]	0.125	1.2	1.4	2.4	3.0	1.0
Radiation Length [cm]	755.2	24.0	14.0	4.9	2.8	36.1
dE/dx [MeV/cm]	0.24	1.4	2.1	3.0	3.8	1.9
Scintillation [γ /MeV]	19,000	30,000	51.300	25,000	42,000	
Scintillation λ [nm]	80	78	128	150	175	

Among all noble elements, the choice of argon as the active medium was made for several reasons. In particular, liquid argon is dense, it does not attach electrons thus allowing a high electron mobility, it is abundant in the atmosphere, it is easy to obtain and to purify. Therefore, liquid argon is the element that presents a good combination of characteristics for the proper functioning of TPC. In addition to all the qualities of liquid argon, one decisive factor for its choice as an active medium is its low price. Remember that active volume of liquid argon in DUNE is 40 kton, therefore, it is important that the material is cheap.

²the speed of light is approximately $v_{\text{light}} \sim 10^8$ m/s, and the drift velocity of the electrons is approximately $v_{\text{drift}} \sim 10^3$ m/s [18].

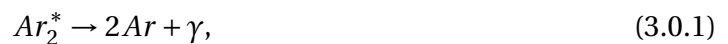
Chapter 3

Scintillation light in LAr

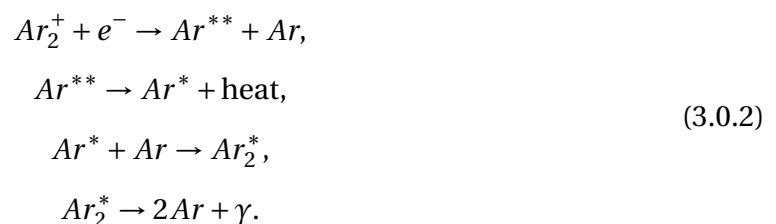
Liquid argon (LAr) is an abundant scintillator and therefore, it is an excellent material to be used in neutrino experiments. For example, for an electric field of 500 V/cm, liquid argon has a light yield of the order of 10^4 photons per MeV of energy deposited in LAr by an ionizing particle. In addition, this material has the characteristic of being transparent to its own scintillation light. Therefore photons can travel long distances in pure liquid argon without being absorbed. Taking into account that current neutrino detectors are getting bigger to increase the probability of interaction, liquid argon transparency is an important feature, since longer drift distances are required.

The passage of charged particles through the volume of liquid argon produces either excited argon molecules (Ar_2^*) or ionized argon molecules (Ar_2^+). Both effects can generate scintillation light in the VUV region (128 nm) due to two processes: *recombination* and *dis-excitation process*, respectively.

The dis-excitation process can be written as



and the recombination one as



Both processes rely on the formation of the excimer's Ar_2^* lowest excited molecular states

$^1\Sigma_u^+$ (singlet state) or $^3\Sigma_u^+$ (triplet state), that decay radiatively into two separated argon atoms in the ground state $^1\Sigma_g^+$ and one photon with a wavelength around 128 nm (9.7 eV), Fig. 3.0.1.

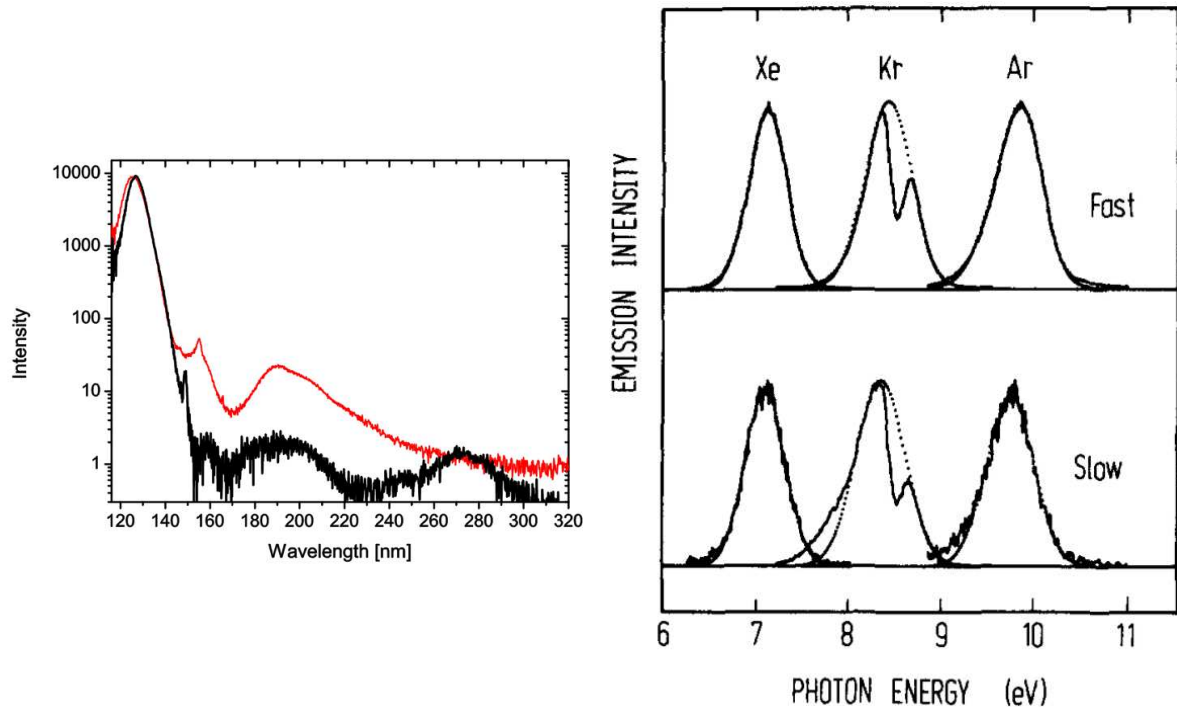


Figure 3.0.1: Left: Emission spectrum of liquid argon at 85 K (black line) and gaseous argon at 295 K (red line) [19]. Right: The emission spectra of both slow and fast components [20].

The dis-excitation from the $^1\Sigma_u^+$ and $^3\Sigma_u^+$ states to the ground state produces two exponentially-decaying components, one with a fast decay constant of a few nanoseconds, τ_s (from $^1\Sigma_u^+$), and the other with a slower one, τ_t (from $^3\Sigma_u^+$), of the order of microseconds.

Therefore, the time evolution of the photon emission can be roughly described by the function

$$I_{\text{scint}}(t) = I_{\text{singlet}}(t) + I_{\text{triplet}}(t) = Ae^{-t/\tau_s} + Be^{-t/\tau_t}, \quad (3.0.3)$$

where $I(t)$ is the intensity of the emitted light, and A and B represent the initial intensities of the fast and slow components respectively.

3.1. Effects of contamination in liquid argon scintillation

3.1.1. Quenching

The processes in Equation 3.0.3 describe the scintillation process in pure argon, but commercial argon usually presents a fraction of impurity (O_2 , N_2 , H_2O and $CO+CO_2$) diluted at ≤ 1 ppm level in LAr. This contamination might cause a scintillation quenching, which is defined as a two-body collision between the argon and the impurities molecules. Taking O_2 contamination as an example, the scintillation quenching can be summarized as



The main consequence of this collision for the scintillation process is the non-radiative dis-excitation of the excimer. Since both recombination and excitation processes rely on the decay of Ar_2^* , there will be less scintillation light in case of quenching. Note that the quenching effect is a two-body collision not fast enough to affect the fast scintillation component. Therefore, mainly the slow component will be affected, as shown in Figure 3.1.2.

The presence of electronegative contaminants affects also the collection of the charge. The concentration of free electrons, $[e^-]$, in the active volume can be related to the concentration of impurities, $[O_2]$, as follows

$$\frac{d[e^-]}{dt} = -k_e[O_2][e^-] \Rightarrow [e^-](t) = [e^-](t=0)e^{-t/\tau_e}, \quad (3.1.2)$$

where the electron lifetime τ_e is defined as

$$\frac{1}{\tau_e} = k_e[O_2] \quad (3.1.3)$$

The value of the electron attachment rate constant k_e depends on the electric field and the kind of contamination, Fig. 3.1.1. In ProtoDUNE-SP, the electron lifetime is measured by three purity monitors from the ICARUS T600 detector, and an electric field of 500 V/cm is used during most of the data acquisition.

The ProtoDUNE-SP purification system only filters out oxygen contamination from the volume of liquid argon. Therefore, it is reasonable to assume that the difference in the lifetime of the electron is mostly caused by the variation in oxygen concentration. In other

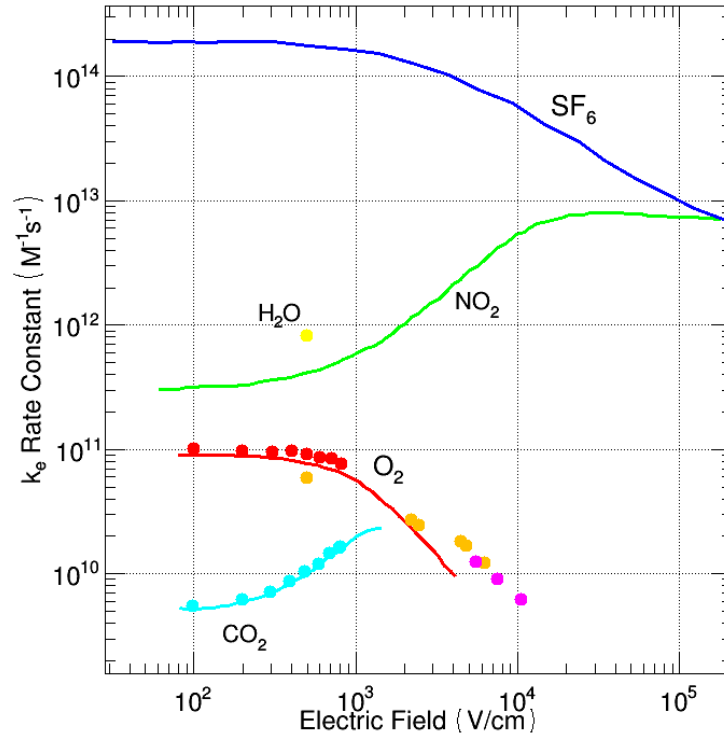


Figure 3.1.1: Electron attachment rate constant in liquid argon for different contamination types [21].

words, the value of the attachment rate constant at 500 V/cm used in Equation 3.1.3 to calculate the oxygen concentration for a given electron lifetime was $k_e = 8.8 \times 10^{10} \text{ M}^{-1} \text{ s}^{-1} = 3.04 \text{ ppm}^{-1} \mu\text{s}^{-1}$, where $M = (\text{mol/L})^{-1}$ [22].

Table 3.1: Properties and relevant information of the liquid argon scintillation light.

Ar ₂ [*] excited dimer states	Singlet ¹ Σu ⁺ , Triplet ³ Σu ⁺
Decay time constants	$\tau_s = 6 \text{ ns}$, $\tau_t = 1.6 \mu\text{s}$
Decay γ Spectrum	$\langle \lambda_{\text{scint}} \rangle = 128 \text{ nm}$
Rate constant @ 500 V/cm for O ₂	$k_e = 3.04 \text{ ppm}^{-1} \mu\text{s}^{-1}$

3.1.2. WArP oxygen contamination test

The effects of oxygen contamination on the liquid argon scintillation light [22] were studied by the Wimp Argon Programme (WArP) collaboration at the Gran Sasso INFN Laboratory (LNGS) in Italy, using two detectors and a wide range of O₂ concentration.

The first detector was a 2.3 L two-phase drift chamber, divided into LAr on the bottom volume and gaseous argon (GAr) on the upper volume. This detector was used for determining the behavior of both ionization electron lifetime and the scintillation slow-component

lifetime during the O_2 purification process. The free electrons were drifted towards the liquid-gas interface due to a vertically-oriented 1 kV/cm electric field. The scintillation light was measured by a set of four 12-stage 3" photomultipliers (PMTs).

Alongside this first prototype, a small dedicated detector, coupled with a system for the injection of controlled amounts of gaseous oxygen was used to study the scintillation light for different O_2 concentrations. This detector was a cylinder ($h = 12$ cm, $\varnothing = 8.5$ cm internal dimensions, wall thickness 0.5 cm) with 0.7L of LAr. A single 2" PMT placed on the open top end of the cell was used to detect the scintillation light induced by γ -sources. Controlled amounts of oxygen were added to the volume of LAr totalling 60 ppb, 300 ppb, 600 ppb, 2 ppm, 5 ppm, 10 ppm. The PMT signal was directly read-out by a fast Waveform Recorder with a sampling time of 1 ns over a full record length of 10 μ s.

By a fitting procedure of the signal shapes, Figure 3.1.2, the long-lived scintillation lifetime τ_t value has been determined. It is possible to notice in Figure 3.1.3 that the behavior of the long-lived scintillation lifetime is constant for a certain range of concentration, and it starts to decrease for concentrations greater than approximately 0.1 ppm.

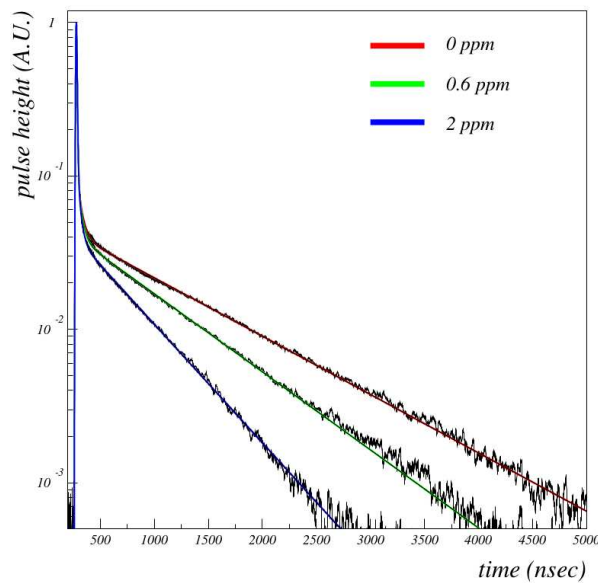


Figure 3.1.2: Example of waveforms for 0 ppm, 0.6 ppm and 2 ppm oxygen contamination [22]. It is possible to notice that all three scintillation fast-component lifetimes coincide, and there is less scintillation slow-component light as contamination increases.

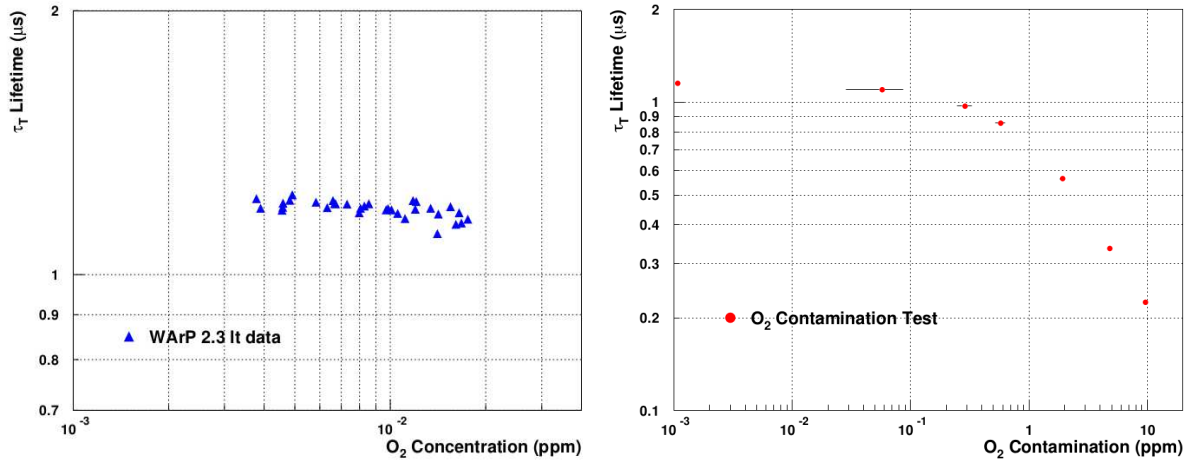


Figure 3.1.3: Slow scintillation light component for different oxygen contamination concentrations for the WArP 2.3 L prototype (left) and the small 0.7 L dedicated detector (right) [22].

3.1.3. Rayleigh scattering and absorption

In addition to the quenching effect described in Section 3.1.1, two other effects can be observed: Rayleigh scattering and absorption. In both cases, the shape of the waveform does not change since those processes are not sensitive to the origin of the photon. The consequence of these effects is that the number of photons that arrive to the photosensitive detector decreases as a whole.

The Rayleigh scattering is an intrinsic property of LAr and it is the process of elastic scattering of light. The wavelength of the light does not change in the scattering process. The well-known expression for the inverse of the Rayleigh scattering length l_R can be found in Landau and Lifshitz [23]. It can be written in the form

$$\frac{1}{l_R} = \frac{\omega^4}{6\pi c^4} \left[kT\rho^2\kappa_T \left(\frac{\partial\epsilon}{\partial\rho} \right)_T^2 + \frac{kT^2}{\rho c_v} \left(\frac{\partial\epsilon}{\partial T} \right)_\rho^2 \right], \quad (3.1.4)$$

where ω is the angular frequency of the radiation, c is the velocity of light, k is the Boltzmann constant, T is the temperature, ρ is the liquid density, κ_T is the isothermal compressibility, c_v is the heat capacity at constant volume, and ϵ is the dielectric constant. The calculation of a Rayleigh scattering length of 90 cm is explicitly derived in the work of G. M. Seidel [24].

Light can also be absorbed by atoms present in the medium while traveling through the material. As argon does not absorb its own scintillation light, Figure 3.1.4, most of the absorption effect is due to the presence of impurities. The absorption length l_A is related to the impurity concentration as follows

$$\frac{1}{l_A} = k_A[\text{O}_2] \quad (3.1.5)$$

where $k_A(\text{O}_2) = 0.034 \pm 0.016 \text{ ppm}^{-1} \text{ cm}^{-1}$ [22] is the photo-absorption coefficient.

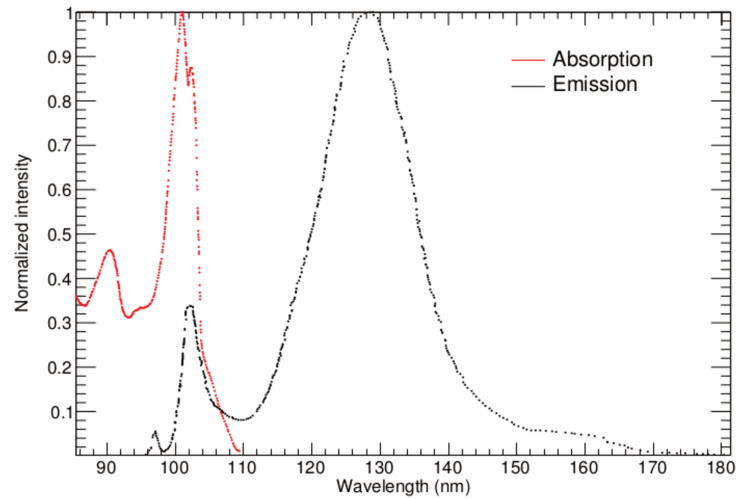


Figure 3.1.4: Emission spectra of argon (black), and absorption spectra of argon (red) . The peaks have been normalized to show the same intensity at the maximum [25, 26, 27].

An accurate value for the Rayleigh scattering length is important to improve simulations. The fact that detectors are getting bigger makes light travel longer distances before its detection.

Chapter 4

The ProtoDUNE-SP experiment

Even though the LArTPC technology has been proven able to meet the Physics goals for DUNE, it is vital that such a relevant, large and expensive detector works as expected to achieve its goals. For this reason, a prototyping and testing program is ongoing to ensure that all parts of the technology are well studied and tested.

The ProtoDUNE experiment [28] is installed at the CERN Neutrino Platform (NP) and will consist of two detectors: (1) the ProtoDUNE-SP that is the single-phase DUNE Far Detector prototype and (2) the ProtoDUNE-DP that is the dual-phase DUNE Far Detector prototype. The latest one is still under construction, while the first one is ready and has been taking data since September 2018. Data from ProtoDUNE-SP will be studied in the present work.

4.1. Charge detection system in ProtoDUNE-SP.

The ProtoDUNE-SP is a 0.77 kton prototype of the 10 kton SP DUNE module, Figure 4.1.1. Its LArTPC of 6 m (height) \times 7 m (width) \times 7.2 m (length) is placed inside a cryostat that maintains the cryogenic temperature of 89 K. A new beamline dedicated to charged-particle tests was used to enable critical calibration measurements necessary for the calorimetry.

The internal volume is divided into two TPCs. One single Cathode Plane Assembly (CPA) is placed in the middle of the internal volume, parallel to the beam direction, and provides a voltage of 180 kV, generating a constant horizontal electric field of 500 V/cm for both TPCs.

The charge readout is performed by the Anode Plane Assembly (APA) located on two of the external walls of the LArTPC. Each APA has three frames of 6.3 m (height) \times 12 cm (width) \times 2.3 m (length) vertically oriented. Two induction planes ($\pm 35.7^\circ$ w.r.t. the vertical) and one

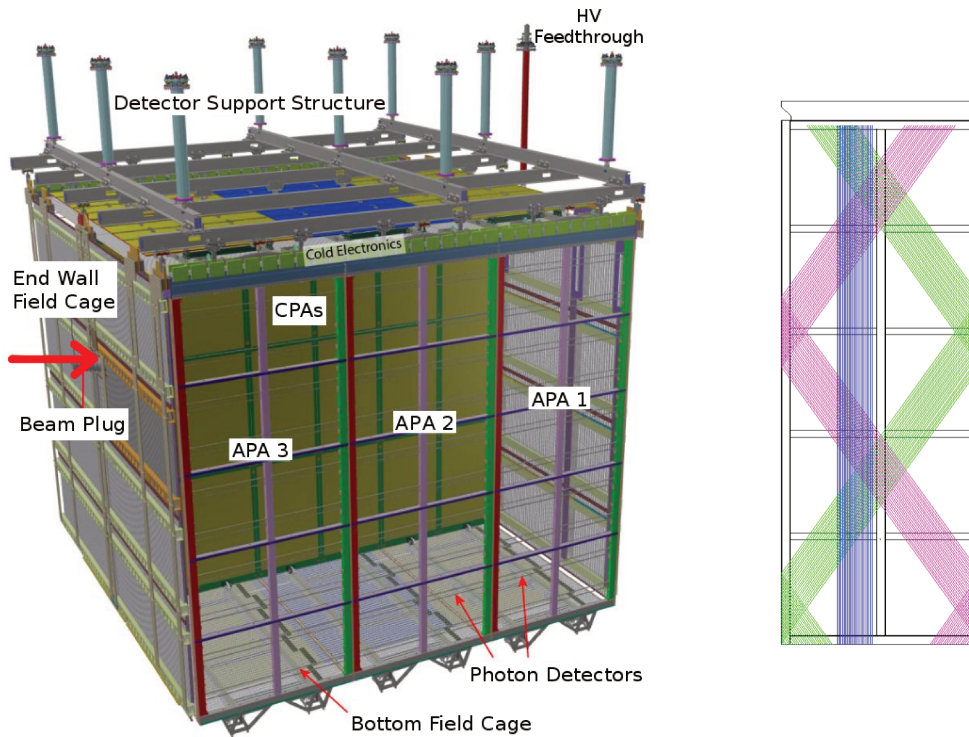


Figure 4.1.1: Left: The major components of the ProtoDUNE-SP TPC. Right: View of the ProtoDUNE-SP wire plane arrangement with two induction layers (green and magenta, $\pm 35.7^\circ$ w.r.t. the vertical) and one collection plane (blue, $\pm 0^\circ$ w.r.t. the vertical) [28].

collection plane ($\pm 0^\circ$ w.r.t. the vertical) compose the frames, Figure 4.1.1.

4.2. Photon detection system in ProtoDUNE-SP

The LAr scintillation light represents roughly half of the deposited energy in the LArTPC and is used for the t_0 determination for non-beam events (fundamental for nucleon decay studies). Many scientists are studying the possibility of using light to extract more information about the event, such as calorimetry. The photodetection system of the ProtoDUNE experiment is testing three different devices¹: ARAPUCA (see Section 4.2.1) and two kinds of light guide bars (see Section 4.2.2 and 4.2.3). Those devices are distributed in six APAs, three in each TPC. The Photon Detection System (PDS) is installed inside an Anode Plane Assembly (APA). As shown in Figure 4.1.1, there are three APAs installed in each TPC. The APA identification system used in this work follows the diagram below:

¹Those devices are in the context of the experiment DUNE, since they fit within the limited space of a few centimeters intended for the installation of the light detection system, unlike traditional PMTs.

Table 4.1: APA identification system according to the DAQ channels. The particle beam enters the TPC on the left side of APA 3, which means that APA 4, APA 5 and APA 6 cannot see the beam signals due to the presence of the cathode dividing the two TPCs. Note that RaS(DaS) stands for Rack Side(DAQ Side) of the TPC.

APA 5 (USDaS)	APA 6 (MSDaS)	APA 4 (DSDaS)
Dip-Coated (ch 216-219)	Dip-Coated (ch 240-243)	Dip-Coated (ch 144-147)
Double-Shifted (ch 220-223)	Double-Shifted (ch 244-247)	Double-Shifted (ch 148-151)
Dip-Coated (ch 224-227)	Dip-Coated (ch 248-251)	Dip-Coated (ch 152-155)
Double-Shifted (ch 228-231)	Double-Shifted (ch 252-255)	Double-Shifted (ch 156-159)
Dip-Coated (ch 192-195)	Dip-Coated (ch 256-259)	Dip-Coated (ch 160-163)
Double-Shifted (ch 232-235)	ARAPUCA (ch 264-275)	Double-Shifted (ch 164-167)
Dip-Coated (ch 196-199)	Dip-Coated (ch 260-263)	Dip-Coated (ch 168-171)
Double-Shifted (ch 200-203)	Double-Shifted (ch 276-279)	Double-Shifted (ch 172-175)
Dip-Coated (ch 236-239)	Dip-Coated (ch 280-283)	Double-Shifted (ch 176-179)
Double-Shifted (ch 204-207)	Double-Shifted (ch 284-287)	Double-Shifted (ch 180-183)

Cathode Plane Assembly

APA 3 (USRaS)	APA 2 (MSRaS)	APA 1 (DSRaS)
Double-Shifted (ch 96-99)	Double-Shifted (ch 48-51)	Double-Shifted (ch 0-3)
Dip-Coated (ch 100-103)	Dip-Coated (ch 52-55)	Dip-Coated (ch 4-7)
Double-Shifted (ch 104-107)	Double-Shifted (ch 56-59)	Double-Shifted (ch 8-11)
ARAPUCA (ch 132-143)	Dip-Coated (ch 60-63)	Dip-Coated (ch 12-15)
Double-Shifted (ch 108-111)	Double-Shifted (ch 64-67)	Double-Shifted (ch 16-19)
Dip-Coated (ch 112-115)	Dip-Coated (ch 68-71)	Dip-Coated (ch 20-23)
Double-Shifted (ch 116-119)	Double-Shifted (ch 72-75)	Double-Shifted (ch 24-17)
Dip-Coated (ch 120-123)	Dip-Coated (ch 76-79)	Dip-Coated (ch 28-31)
Double-Shifted (ch 124-127)	Double-Shifted (ch 80-83)	Double-Shifted (ch 32-35)
Dip-Coated (ch 128-131)	Dip-Coated (ch 84-87)	Dip-Coated (ch 36-39)

4.2.1. ARAPUCA

ARAPUCA (Argon R&D Advanced Program at UniCAmp) [29] is a new device for the detection of the scintillation light of liquid argon (128 nm wavelength in the VUV²). This device is a box made of very high reflective internal walls. One of the walls is an acceptance window, through which the light enters the device. The combination of a dichroic filter and two wavelength shifters (deposited on the two faces of the filter) for the acceptance window trap the photons. The trapped photons are reflected by the internal surfaces of the device until their detection by a Silicon Photomultiplier (SiPM) located on one side wall.

A dichroic filter with a cutoff of 400 nm ($\lambda_{\text{cutoff}} = 400 \text{ nm}$) has been used for the accep-

²Vacuum Ultra Violet.

tance window. It means that the filter is transparent (transparency $> 95\%$) to light with wavelength below λ_{cutoff} , and reflective (reflectivity $> 98\%$) to light with wavelength above λ_{cutoff} . Both wavelength shifters were wisely chosen to create a photon trap. p-Therphenyl (PTP) was deposited on the outer surface (S_{outer}), and Tetraphenyl Butadiene (TPB) on the inner surface. This configuration allows the device to trap the light since the shifters' emission wavelength obey $\lambda_{\text{PTP}} < \lambda_{\text{cutoff}} < \lambda_{\text{TPB}}$, Fig. 4.2.1. In other words, the light emitted by the first shifter, PTP, will pass the filter, while the light emitted by the second shifter, TPB, will be reflected by it.

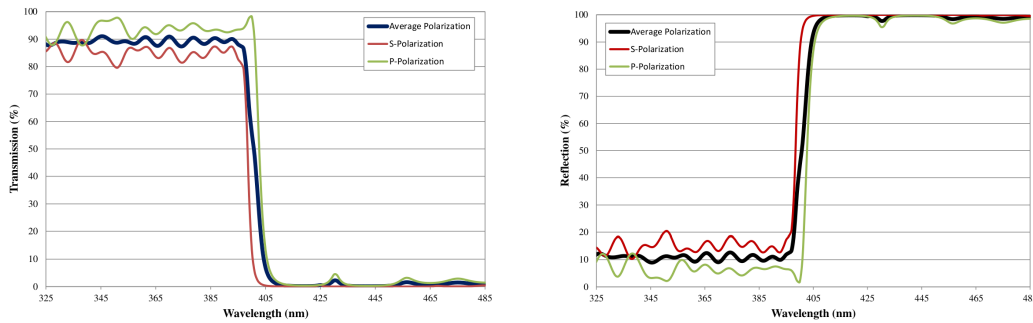


Figure 4.2.1: Dichroic filter transmission (left) and reflection (right) [30].

The scintillation light travels through the volume of liquid argon and first interacts with the outer shifter PTP. Its wavelength is converted from 128 nm to 350 nm. Because PTP's emission wavelength is below the λ_{cutoff} , the emitted light passes the filter and interacts with the second shifter TPB. Now the light wavelength is converted from 350 nm to 430 nm, which is above λ_{cutoff} , and therefore light is reflected back into the box.

This device has been installed and tested in many different experiments. The configuration installed in ProtoDUNE-SP consists of two arrays composed of sixteen ARAPUCA cells, Figure 4.2.2, each cell with dimensions of 8 cm \times 10 cm. The readout system is made using a SiPM with active dimensions 0.6 cm \times 0.6 cm. Half of the cells have 12 SiPMs installed on the bottom side of the cell and half have six SiPMs, which corresponds respectively to a total active dimension of 5.6% and 2.8% of the area of the window (7.8 cm \times 9.8 cm).

Each set of 12 SiPM is associated to one readout channel, which means that ARAPUCAs with 12 SiPMs are connected to one channel individually, and two ARAPUCAs with six SiPMs each are connected in parallel to one channel.

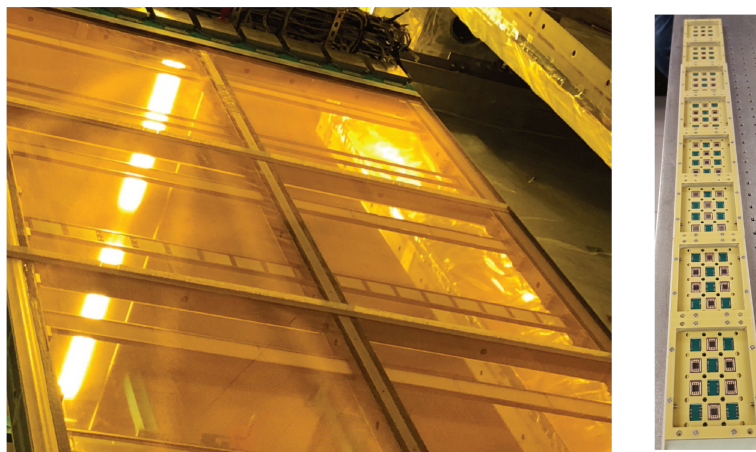


Figure 4.2.2: ARAPUCA array in ProtoDUNE-SP [13].

4.2.2. Dip-coated light guides

The dip-coated light guides, Figure 4.2.3, have a mechanism very similar to an optical fiber. To make it possible to detect the light, the VUV scintillation light is wavelength-shifted to ~ 430 nm due to a layer of TPB coated on the surface of the bar. Total internal reflections guide the wavelength-shifted light towards the array of SiPM installed at one edge of the bar.

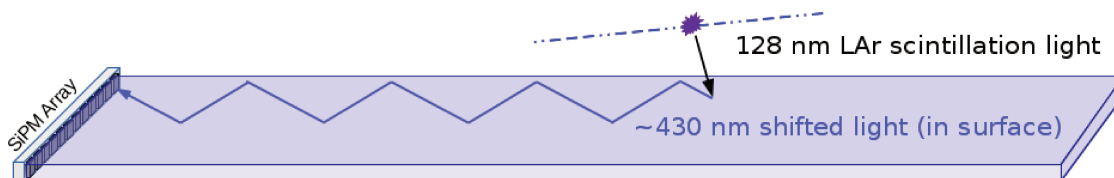


Figure 4.2.3: Schematic of scintillation light detection with dip-coated light guide bars (Ref. [13]).

4.2.3. Double-shift light guides

Similarly to the dip-coated light guides, Figure 4.2.4, the double-shift ones guide the light through total internal reflections towards an array of SiPM installed at one edge of the bar. The difference is that light is wavelength-shifted twice, and this mechanism has been implemented to decrease the impact of the coating on the total internal reflection efficiency, which is a problem for the dip-coated light guides.

A spray-coating layer of TPB on the outer surface of the acrylic bar wavelength-shifts the VUV scintillation light to ~ 430 nm. The second wavelength-shift is caused by 12 layers

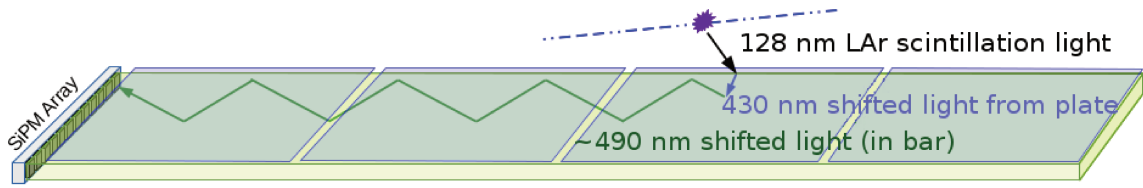


Figure 4.2.4: Schematic of the double-shift light guide concept [13].

of polystyrene bars doped with the EJ-280 wavelength shifter, whose absorption spectrum matches the TPB emission spectrum, and remits the absorbed light to a wavelength of ~ 490 nm.

A comparison of the properties of the light detection devices is displayed on the table below:

Table 4.2: Information about the optical properties of each light detection device installed in the ProtoDUNE-SP experiment. Hamamatsu (HMM) and Sense Light (SensL) SiPMs were used.

Device	Light Trapping	Light Detection
ARAPUCA	PTP + dichroic filter + TPB	HMM SiPM
Dip-coated light guide	TPB	HMM SiPM
Double-coated light guide	TPB + EJ-280	SensL SiPM

The dimensions of the bars are $209.3 \text{ cm} \times 8.47 \text{ cm} \times 0.60 \text{ cm}$.

4.3. Silicon photomultiplier

All three light detectors in the ProtoDUNE experiment use silicon photomultipliers to detect light. As well as the traditional photomultipliers, SiPMs are responsible for transforming the incident light signal into an electronic signal.

A SiPM consist of an array of multiple single avalanche photodiodes operated in Geiger mode. Each component or pixel produces a pulse of constant amplitude regardless of the number of incoming photons. All pixels are connected to the same output channel providing a total output signal equal to the sum of those from the individual pixels. There is a probability that an avalanche caused by an incident photon in a pixel can trigger neighboring pixels, resulting in an artificial increase in signal [31]. This effect is called *crosstalk*.

A second possible effect is called *afterpulse*. An afterpulse happens during an avalanche, when carriers can become trapped in defects in the silicon, being released only after a period

of time resulting in a delayed pulse [32].

4.4. Calibration

The calibration is an essential step for a detector because it associates the readout signal with the incoming information. In particular, the calibration of the photon detection system consists of finding the signal generated by the detection of a single photon by the light sensitive devices. More specifically, the calibration consists of calculating the area³ of the pulse⁴ generated by this detected photon.

A careful study of single photon pulses was done. This study used light coming from a LED configured to generate few photons at a time⁵. Each waveform consists of a set of 2,000 ticks distant 6.67 ns from each other, a total information window of 13.3 μ s.

A process of smoothing was performed twice on each waveform before the integral calculation. First a *moving average* was done using the eight ticks adjacent to each tick (four on each side). Moving average is a process that calculates the average value of subsets within the full data set, in this case, four on each side. A moving average of M adjacent points can be generalized as

$$\bar{y}(x_n) = \frac{1}{2M+1} \sum_{i=-M}^M y(x_{n+i}). \quad (4.4.1)$$

The value of M must be updated for each point since the number of adjacent points varies as follows. Considering a set of N points, M follows as

Points	x_0	x_1	x_2	x_3	x_4	x_5	x_6	\dots	x_{N-5}	x_{N-4}	x_{N-3}	x_{N-2}	x_{N-1}
M	0	1	2	3	4	4	4	\dots	4	3	2	1	0

Second, a *total variation denoising* algorithm [34] was used to decrease the noise in the signal. Given a noisy signal, $y = (y[1], \dots, y[N])$, the denoised signal, $y_{den} = (y_{den}[1], \dots, y_{den}[N])$, is defined implicitly as the solution to the minimization problem

$$\underset{x \in \mathbb{R}^N}{\text{minimize}} \quad \frac{1}{2} \sum_{k=1}^N |y[k] - y_{den}[k]|^2 + \lambda \sum_{k=1}^{N-1} |y_{den}[k+1] - y_{den}[k]| \quad (4.4.2)$$

for some regularization parameter $\lambda \geq 0$. The final denoised signal is shown in Figure 4.4.1.

³This area is also called *charge*.

⁴This pulse is also called *waveform*.

⁵This set of data is called DUNE Calibration Module (DCM) data run [33]

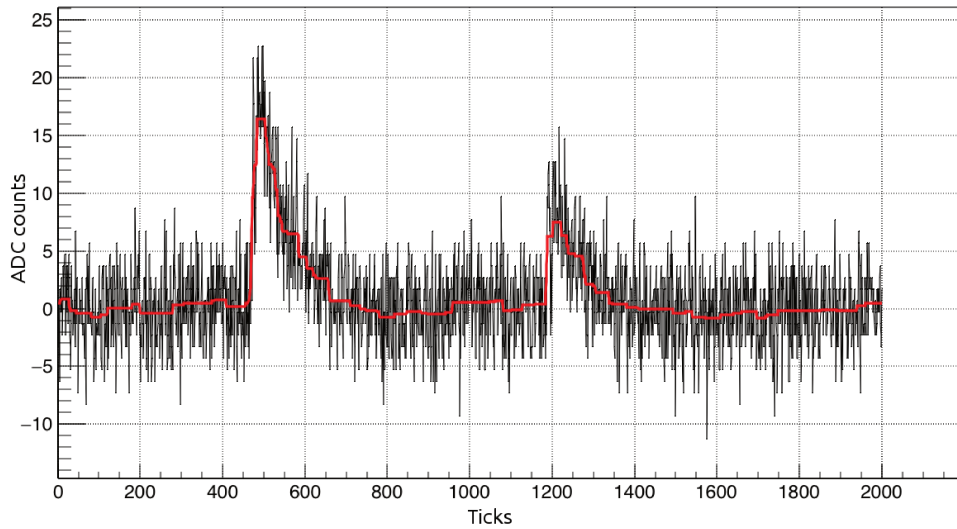


Figure 4.4.1: An example of the smoothing process, in which it is possible to see the raw data (black line) and the smoothed one (red line), using the combination of the moving average and the total variation denoising algorithm.

Two windows were mainly used for the calibration process. First, the [0:1000] ticks were used to evaluate the baseline, second, the [1000:1500] ticks were used to calculate the integral of the signal.

The SiPM used in ARAPUCA device has a linear behavior, which means that the integral of the pulse of n photoelectrons (cells) is n times the integral of the pulse of one photoelectron (cell). This behavior is evident when the integrals are displayed in a histogram, see Figure 4.4.2.

The first peak of Figure 4.4.2 represents the baseline, resulting from the integration of empty waveforms, while the others represent the integral of $n = 1, 2, 3, \dots$ photons. The center value of each peak was obtained from the fit of a Gaussian. For a matter of nomenclature, from now on the integral for one photoelectron is going to be referenced as SPE_{integral} .

From the histogram in Figure 4.4.2, it is possible to recover the integral of a signal generated by one photoelectron. However, the total integral measured for N detected photons is greater than $N \times SPE_{\text{integral}}$ due to the crosstalk and afterpulse effects. So corrections have to be made taking into account crosstalk and afterpulse effects. In DCM runs, photons are emitted by a LED. Assuming that the emission of these photons follows a Poisson distribution, the probability of having n photons is given by

$$P(n) = \frac{\lambda^n e^{-\lambda}}{n!}, \quad (4.4.3)$$

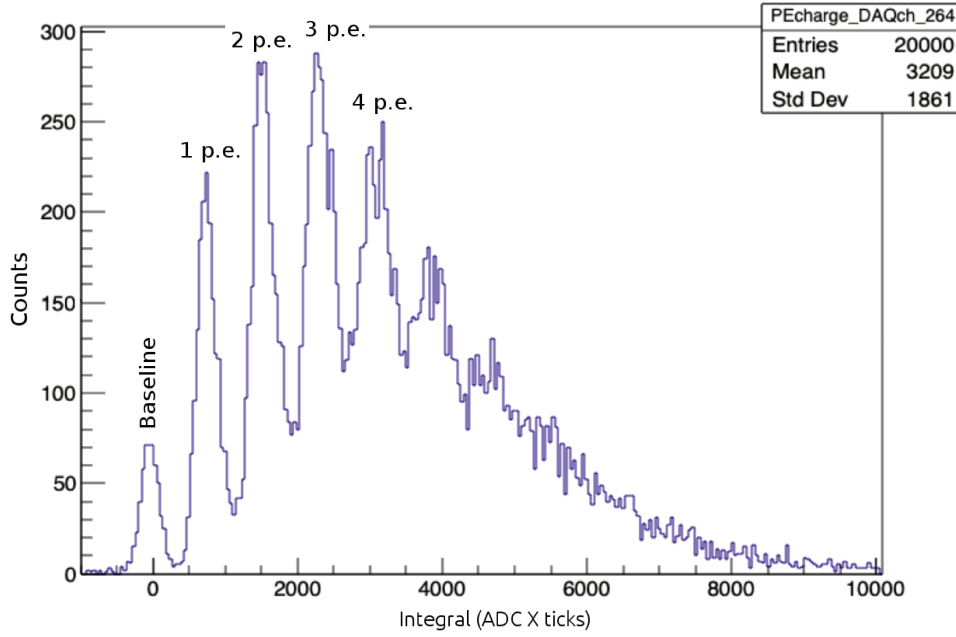


Figure 4.4.2: Histogram of the integral of the signal for channel 264. The first peak centered in zero represents the integral of empty waveforms, in other words, it is the baseline peak. The consecutive equally-spaced peaks represent the integrals of the multiple integers of photoelectrons (p.e.).

where λ

$$\lambda = -\ln\left(\frac{n(0)}{n_{\text{total}}}\right) \quad (4.4.4)$$

is the rate parameter and represents the average number of photons per waveform, $n(0)$ is the expected number of events when zero photons are detected, and n_{total} is the total number of events. So, the ratio between the total measured charge and the total expected charge

$$\frac{Q_{\text{measured}}}{Q_{\text{expected}}} = \frac{\langle \bar{Q} \rangle}{\lambda \times SPE_{\text{integral}}} \equiv n_{\text{eff}} \quad (4.4.5)$$

represents the crosstalk rate, where $n_{\text{eff}} = 1$ in the absence of the crosstalk effect, and $n_{\text{eff}} > 1$ otherwise. In other words, on average a signal of n_{eff} photons is being detected per incident photon, and for this reason it is reasonable to use

$$Q_{\text{corrected}} = \frac{\langle \bar{Q} \rangle}{\lambda} = n_{\text{eff}} \times SPE_{\text{integral}} \quad (4.4.6)$$

as the charge generated by each detected photon. The final calibration with and without the corrections are shown in Table 4.3.

Table 4.3: Calibration for the ARAPUCA channels on the APA 3. The calibration is given in $\text{ADC} \times \text{ticks}$ and the calibration with correction takes into account crosstalks.

DAQ Channel	Calibration (1st peak)	n_{eff}	Calibration (w/ correction)
132	782 ± 7	1.479	1157 ± 10
133	750 ± 5	1.437	1078 ± 7
134	780 ± 6	1.415	1104 ± 8
135	783 ± 10	1.445	1131 ± 14
136	812 ± 7	1.472	1196 ± 10
137	665 ± 1	1.313	873 ± 1
138	737 ± 10	1.435	1057 ± 14
139	631 ± 2	1.378	869 ± 3
140	673 ± 10	1.263	850 ± 13
141	628 ± 9	1.277	802 ± 11
142	790 ± 13	1.178	930 ± 15
143	798 ± 14	1.273	1016 ± 18

By knowing the signal generated by a single detected photon, it is possible to calculate the total number of incident photons at each light detector for an event inside the TPC. The total number of incident photons is calculated dividing the area of the signal pulse for one event by the calibration (with correction) value for each detector. This precise proceeding was used in Section 6.2 to calculate the total number of incident photons at the ARAPUCA module for an electron beam of 0.5 GeV entering the TPC.

Chapter 5

Data Selection

5.1. Data acquisition

The process of data acquisition in the ProtoDUNE-SP experiment can be mainly characterized as physics run or as cosmic run. For the sake of nomenclature, *physics run* refers to the set of data taken in the presence of the particle beam, whereas *cosmic run* refers to the set of data taken in the absence of the particle beam.

For both physics and cosmic runs, a combination of self-triggered (also called internal trigger) and externally triggered events make up the Photon Detection System (PDS) data. The external trigger for physics runs comes from the beam instrumentation that provides a trigger signal every time there is a particle entering the TPC. The external trigger for cosmic runs comes from the Cosmic Run Tagger (CRT). The CRT is made up of segmented scintillator-strip modules, vertically installed perpendicularly to the beam direction, as shown in Figure 5.1.1. The segmentation allows identifying the points in which the particle crossed the module and reconstructing the trajectory by combining the points.

On the other hand, the self-triggered events are the same for both physics and cosmic runs. The self-triggered data are induced by cosmic rays, and only waveforms with an amplitude greater than a specific threshold are captured.

Regardless of the trigger type, the un-amplified analog signals from the SiPMs are transmitted directly to outside the cryostat and read by a module called SiPM Signal Processor (SSP). Once there is an external trigger, a waveform is saved. At the same time, a waveform is saved for every internal trigger that occurs within a data acquisition window of 2.75 ms around the time of the external trigger. The self-triggered signals can be used to estimate the

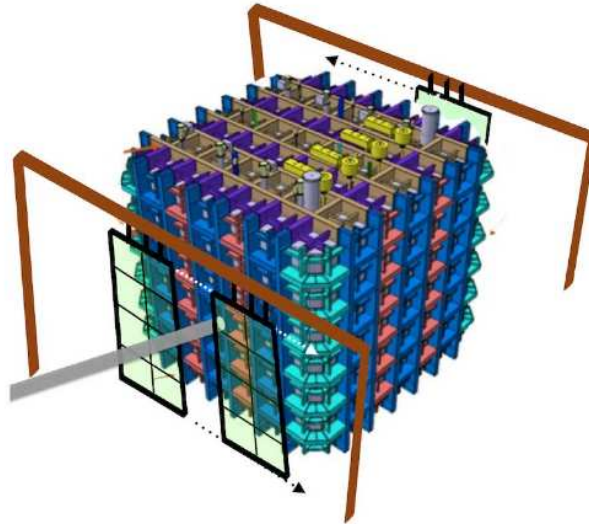


Figure 5.1.1: Cosmic Run Tagger design for ProtoDUNE-SP. The position of the modules allows identifying events from cosmic rays parallel to the beam [28].

background for the external trigger event. The time frame of the data collection is shown in Figure 5.1.2.

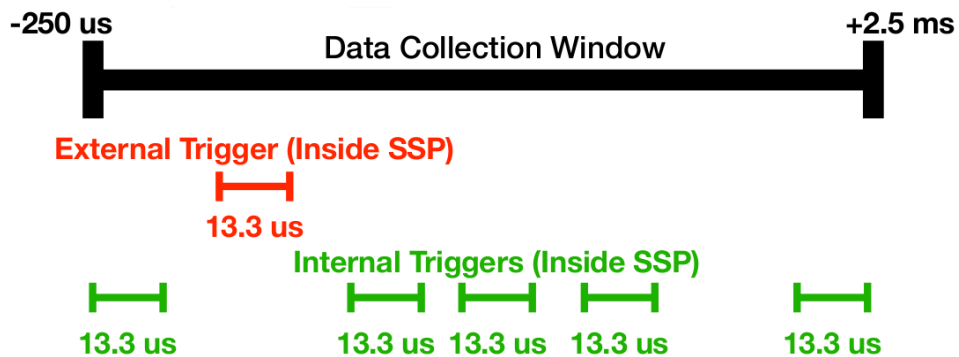


Figure 5.1.2: Scheme of the photon detection system for data collection after an external trigger.

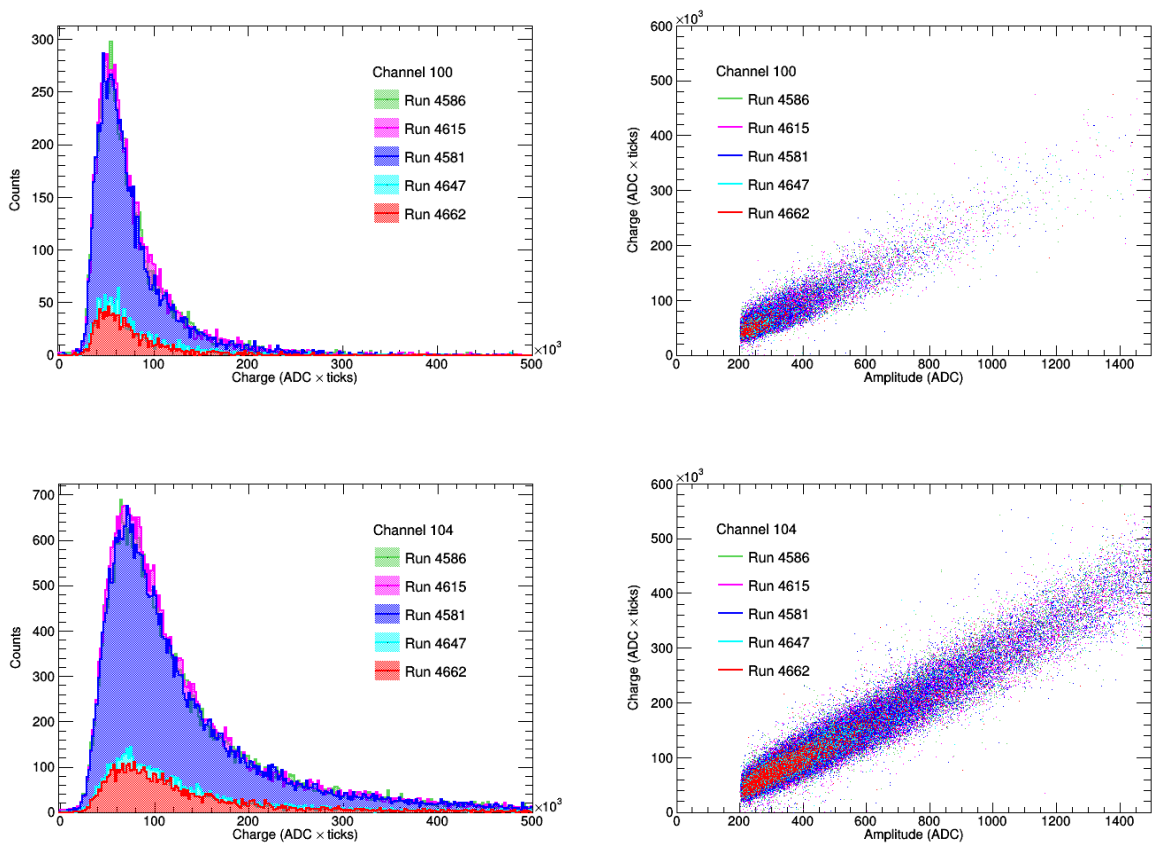
5.2. Internal Trigger

Since the internal trigger only saves the data above a certain threshold, one should always be careful when analyzing those data. This section aims to show that the internal trigger adds a bias to the self-triggered data of the ProtoDUNE-SP experiment. In other words, the data collected from the internal trigger does not represent the total set of data.

The histograms in Figure 5.2.1 show the charge spectrum¹ collected for runs with a constant threshold of 200 ADC, see Table 5.1. One can notice that the threshold abruptly cuts the distribution of the plots to the right in Figure 5.2.1. The charge distribution in Figure 5.2.2 shows how the threshold changes the distribution and can lead to wrong conclusions. For this example, data from run 4573 was used, whose threshold was 100 ADC.

Table 5.1: Information on the runs used for the energy spectra shown in Figure 5.2.1.

Date	Run Number	Run Type	τ_e (ms)	[O ₂] (ppb)	Threshold (ADC)
09/21/2018	4581	cosmics	0.046	7.15	200
09/22/2018	4586	cosmics	0.057	5.77	200
09/23/2018	4615	cosmics	0.062	5.31	200
09/24/2018	4647	cosmics	0.073	4.51	200
09/25/2018	4662	cosmics	0.108	3.05	200



¹Charge is equivalent to integral in this context. Therefore, *charge spectrum* means exactly the same as *integral spectrum*, which is the histogram of the integral of each waveform.

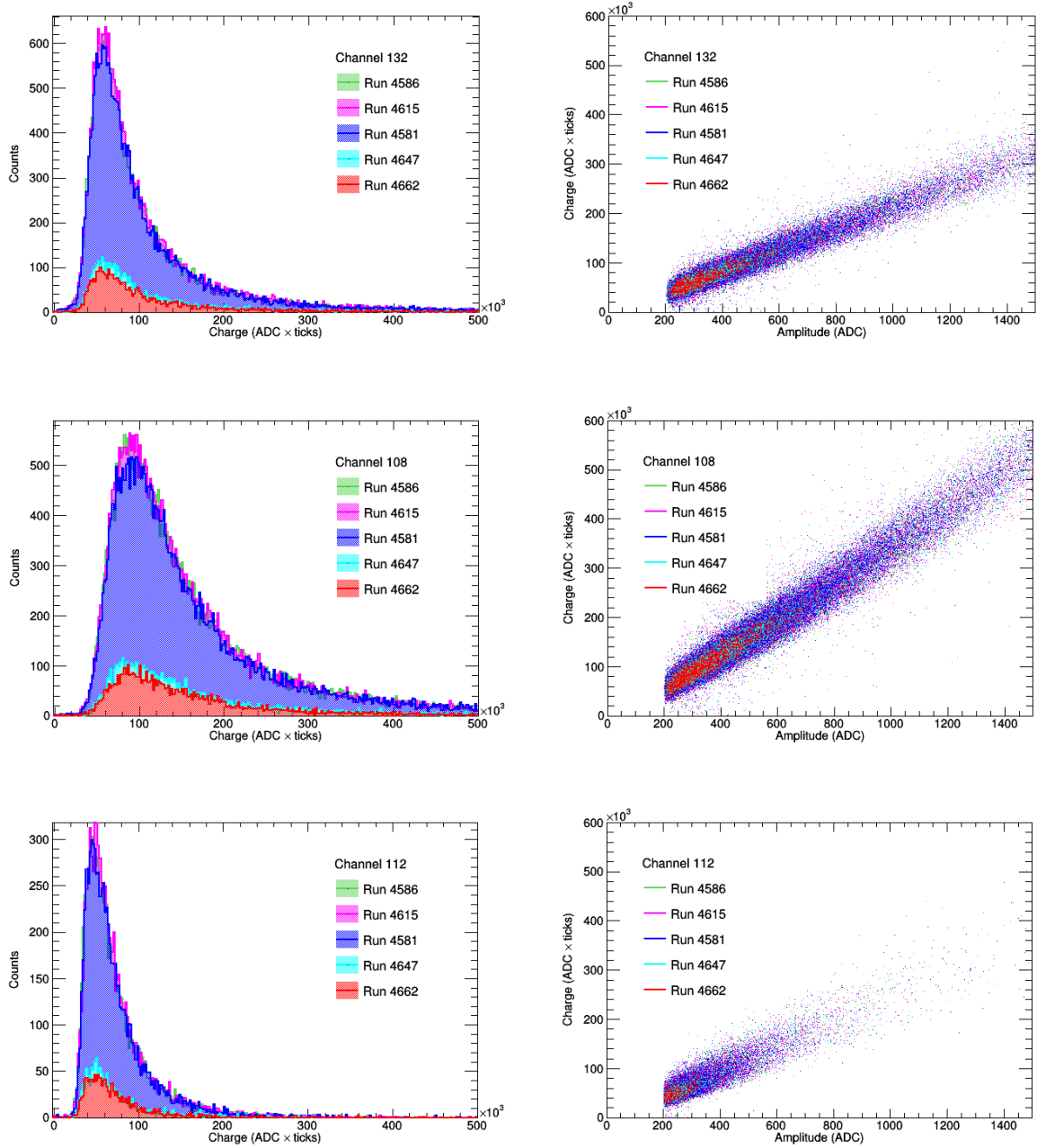


Figure 5.2.1: Charge spectrum histograms for internal trigger data in cosmic runs. The distributions for channels 100, 104, 132, 108 and 112 are displayed. The difference in the number of entries of each run is due to the fact that they do not have the same duration and, therefore, they have not collected the same amount of data.

Even though the threshold requires careful attention, it is possible to notice the expected linear response of the SiPM.

5.2.1. Data sample for internal trigger

The data used to analyze the behaviour of the waveform shape as a function of the purity were taken during the liquid argon purification process in the ProtoDUNE-SP experiment.

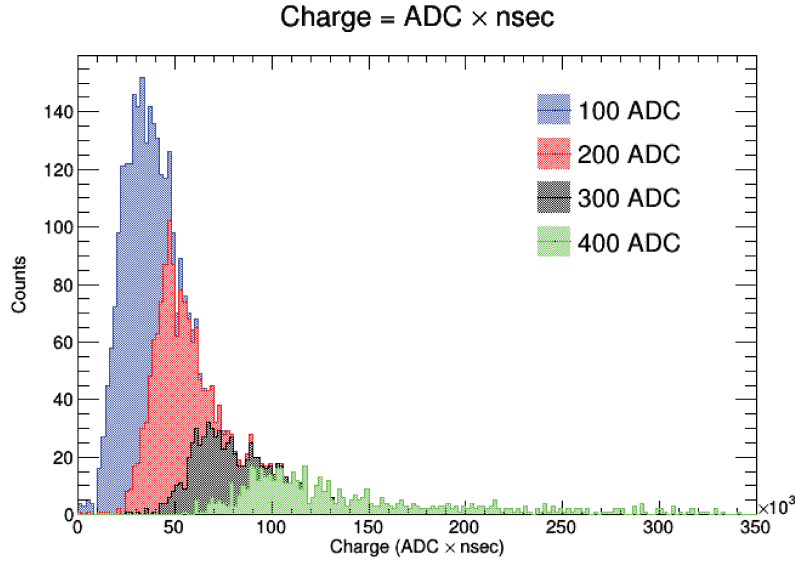


Figure 5.2.2: Charge spectrum histogram for internal trigger data in cosmic runs, using different thresholds for run 4573 and channel 132.

Three purification monitors, inherited from the ICARUS T600 experiment [35], were used in the ProtoDUNE-SP experiment. Each monitor was installed at a different height from the TPC: bottom, middle, and top. The measured electron lifetime and the calculated oxygen concentration are displayed in Figure 5.2.3. The reason for the disagreement of the electron lifetime measurements among different monitors is under investigation.

The four falls in purity present in Figure 5.2.3 were due to possible conditions that resulted in the failure of the purification pumps, such as power outage.

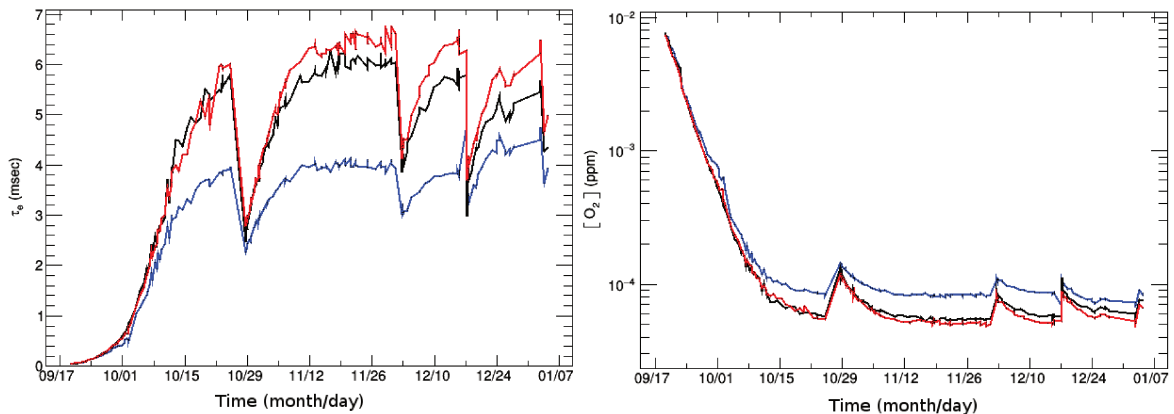


Figure 5.2.3: Electron lifetime and oxygen concentration in ProtoDUNE-SP from September, 2018, to January, 2019. The oxygen concentration was calculated using Equation 3.1.3 and the constant rate for oxygen at 500V/cm. The electron lifetime was measured using three purity monitors from the ICARUS T600 detector [35] installed at the top (red), middle (black) and bottom (blue) of the TPC. Note that the concentration varies over time making it crucial to understand if light is affected by this variation.

To verify how the variation of the oxygen concentration affects the slow-time decay of the scintillation light, it was necessary to analyze data from the beginning of the data acquisition, Figure 5.2.3. According to the studies done by the WArP collaboration, the slow component of scintillation of argon is sensitive to contamination above 0.1 ppm.

Another important factor that needs to be taken into account is that the shape of the scintillation light signal depends on the type of particle that is generating it, as shown in Figure 5.2.4.

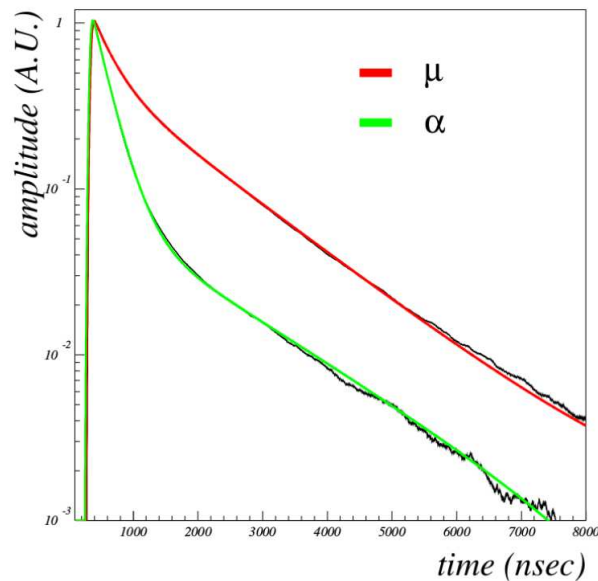


Figure 5.2.4: LAr scintillation light waveform caused by the passage of an alpha (green) and muon (red) particles into liquid argon [36].

Unfortunately, by the time of this dissertation, particle ID tools were not yet available for ProtoDUNE-SP data, therefore it was not possible to explore a wide range of particle samples. If the CRT reconstruction were available for the ProtoDUNE data, it would be possible to reconstruct the muons crossing the TPC volume and select those passing close to the photosensitive devices, to make sure that the signal analyzed was from a muon, but this tool was also not yet available.

As explained previously, internal triggered data for both cosmic and beam runs are used to save waveforms of particles crossing the TPC in a time window around the external trigger. Therefore, in the absence of an external trigger (caused by beam or horizontal cosmic rays) the activities inside the detector are mainly due to cosmic rays and radioactivity action. The energy deposited by radioactivity action is much smaller than the one deposited by cosmic rays. So, we are assuming that internal trigger signals are mostly cosmic ray signals.

5.2.2. Cosmic rays at sea level

The ProtoDUNE-SP is installed at the CERN Neutrino Platform, which is a building at the surface. For this reason, a high flux of cosmic rays of 10 kHz is expected in the detector.

Cosmic rays [37, 38] are atomic nuclei that enter the atmosphere and collide mainly with oxygen and nitrogen atoms present in the air. Such collisions produce lighter particles, and the set of such particles constitutes an air shower. Figure 5.2.5 shows the flux at sea level (altitude of 0 km) of different particles produced from cosmic rays.

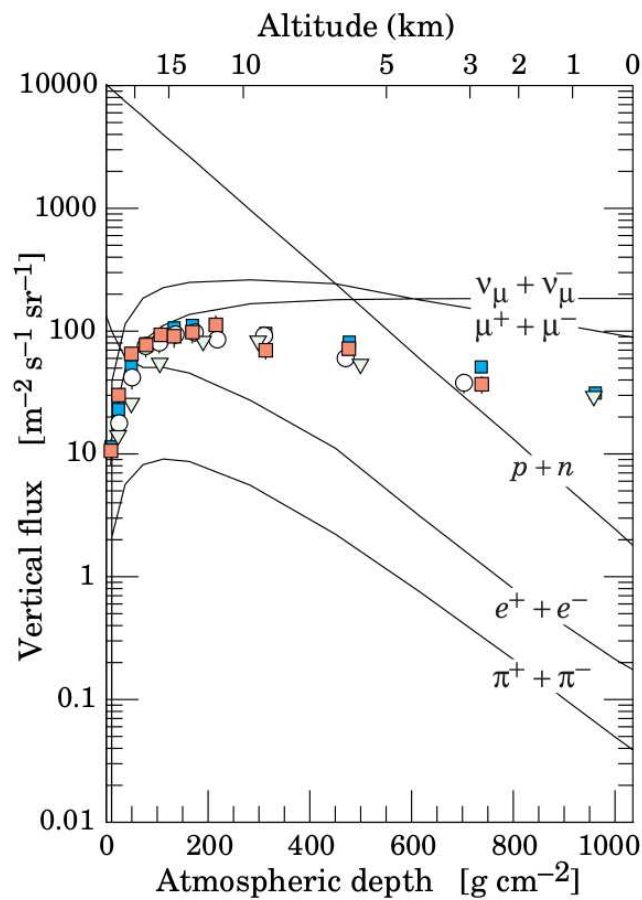


Figure 5.2.5: Vertical flux of cosmic rays at different altitudes [7].

Therefore, analyzing data from cosmic rays at sea level (atmospheric depth of 1000 g cm^{-2}) mainly means to be analyzing muons, and particle ID selection is important for the study of the decay time for the slow LAr scintillation light component. For this reason, this analysis was done using self-triggered data.

5.2.3. Signal modelling

To study how the contamination was affecting the slow component of the liquid argon scintillation light, a signal model was created considering some features. First of all, the emission of the scintillation light of liquid argon occurs in two exponentially-decaying components, one with a fast decay constant, and the other with a slower one, according to Equation 3.0.3.

The second consideration that should be taken into account is the fact that the TPB used to shift the wavelength has an exponentially delayed light emission [39] that follows

$$I_{\text{delayed}}(t) = \eta_S \frac{N}{[1 + A \ln(1 + t/t_a)]^2 (1 + t/t_a)}, \quad (5.2.1)$$

where N and A are constants depending on the nature of the scintillator, η_S is the fluorescence yield, and t_a is the relaxation time that is linked to the diffusion coefficient of the triplet state in the scintillator.

For statistical reasons, the SiPM response adds a time convolution with a normalized Gaussian to the final waveform, like

$$G(t) = \frac{1}{\sqrt{2\pi}a} \exp\left(-\frac{(x-b)^2}{a^2}\right), \quad (5.2.2)$$

where a is the standard deviation and b is the position of the center of the peak. Therefore, the fit will be done in a waveform $WF(t)$ of the form

$$WF(t) = G(t) * [I_{\text{scint}}(t) + I_{\text{delayed}}(t)]. \quad (5.2.3)$$

An easy example of how the waveform is changed due to Equations 5.2.1 and 5.2.3 is shown in Figure 5.2.6. The time contribution that the detector response adds to the final signal is cumulative. Each point in time contributes a Gaussian of the same amplitude of the signal, and the final amplitude after convolution will be the sum of all Gaussians prior to this point since they are time oriented. This is illustrated in Figure 5.2.6 to the right.

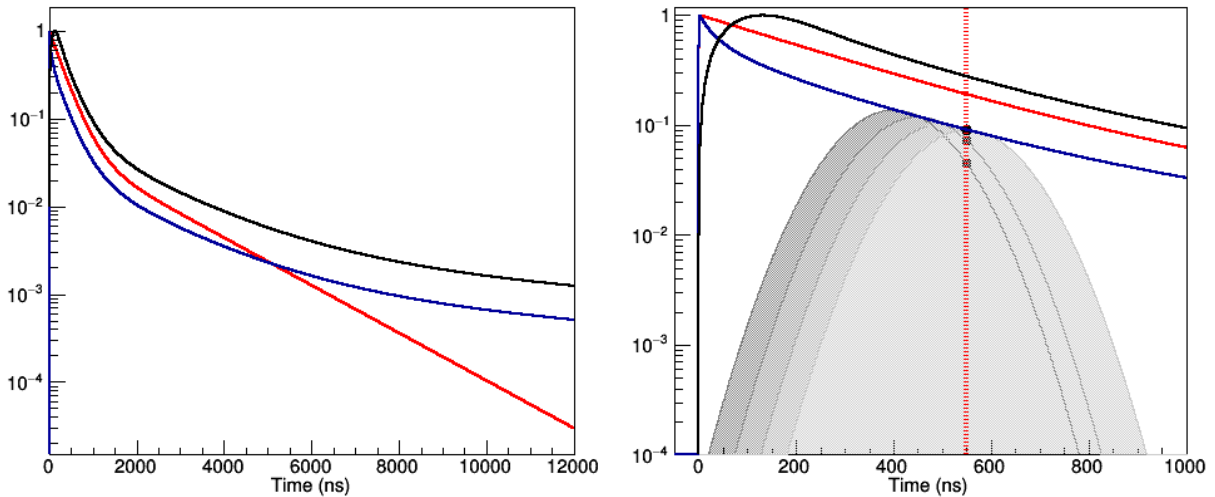


Figure 5.2.6: (Left) Waveforms for three different configurations: LAr scintillation light (red), LAr+TPB scintillation light (blue) and LAr+TPB scintillation light convoluted with the normalized Gaussian (black). (Right) Example of how the convolution is calculated. The convolution result is the sum of all the contributions from the Gaussian before that point. The amplitude of all three curves are normalized to be equal to 1 in both plots.

5.3. Beam external trigger

The beam data was used to analyze the Rayleigh scattering effect due to the purity difference of the liquid argon. To verify the effect of Rayleigh scattering, a particle beam with a momentum of 0.5 GeV was analyzed for two different purities. A combination of instrumentation allows identifying the particles in the beam. Due to the momentum value of the beam, the production of electrons and pions dominates. The identification of these particles is done with the help of two detectors located along the beam: time of flight and the low-pressure Cerenkov detector.

Table 5.2: Selected beam run information. The electron lifetime was measured using the monitor 1, that is close to the ARAPUCA array in APA 3. For both cases, the TPC cathode voltage was 180 kV and the ARAPUCA bias voltage was 48 V.

Run Number	Date	Electron Lifetime	Beam Energy
4878	October 2nd, 2018	0.605 ms	0.5 GeV
5837	November 11th, 2018	5.775 ms	0.5 GeV

Chapter 6

Signal Analysis

6.1. Quenching analysis

The analysis of the decay time for the slow LAr scintillation light component was made using average waveforms for a fixed condition, which means, a fixed run number. A fit using the idealized signal described in Section 5.2.3 and the ROOT function called TMinuit was done individually for each average waveform.

6.1.1. Average Waveform

A common practice used in noisy data analysis is the use of the average signal. This practice reduces the effect of random noises present in the data. To reduce once more the contribution difference between small and big pulses, the waveform was normalized by its integral before being summed up to the total average waveform. Only self-triggered pulses were considered for the following analysis. The analyzed runs are shown in Table 6.1.

Table 6.1: Run selection for the analysis of the average waveform. Those runs were selected due to their oxygen concentration.

Date	Run Number	τ_e (ms)	[O ₂] (ppb)
4583	09/21/2018	0.046	7.137
4588	09/22/2018	0.057	6.335
4614	09/23/2018	0.062	5.333
4634	09/24/2018	0.079	4.501
4663	09/25/2018	0.107	3.059
4712	09/26/2018	0.129	2.531

The evaluation of the baseline was done individually using the first 30 ticks of each waveform. A noticeable electronic effect on the light signals detected on all light detectors is the *undershoot*, as exemplified in Figure 6.1.1, in which the signal does not return to the baseline value after the pulse. After the baseline subtraction, both areas above and below the baseline were calculated to check the undershoot effect. The negative area was around 2%(7%) of the positive one for the bars(ARAPUCAs). Therefore, the undershoot effect is clearly more significant for the ARAPUCAs channels.

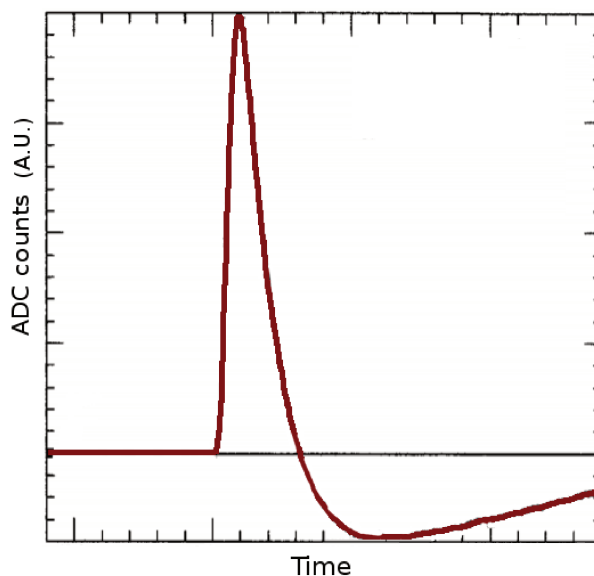


Figure 6.1.1: Example of an undershoot. The undershoot effect shown in this figure is exaggerated from that observed in the experimental data of the ProtoDUNE-SP experiment.

The current analysis was made using some photosensitive devices installed on the APA 6. The selection of the channels was done intentionally, so that two channels of each technology were analyzed, as shown in Table 6.2.

Table 6.2: Selection of the channels for the analysis of the slow scintillation component of liquid argon.

Technology	DAQ Channels
Double-Shifted Light Guide	252 and 253
Dip-Coated Light Guide	257 and 258
ARAPUCA (6 SiPM)	264 and 265
ARAPUCA (12 SiPM)	268 and 268

The final average waveforms per channel and per run are shown in Figure 6.1.2 to Figure 6.1.5.

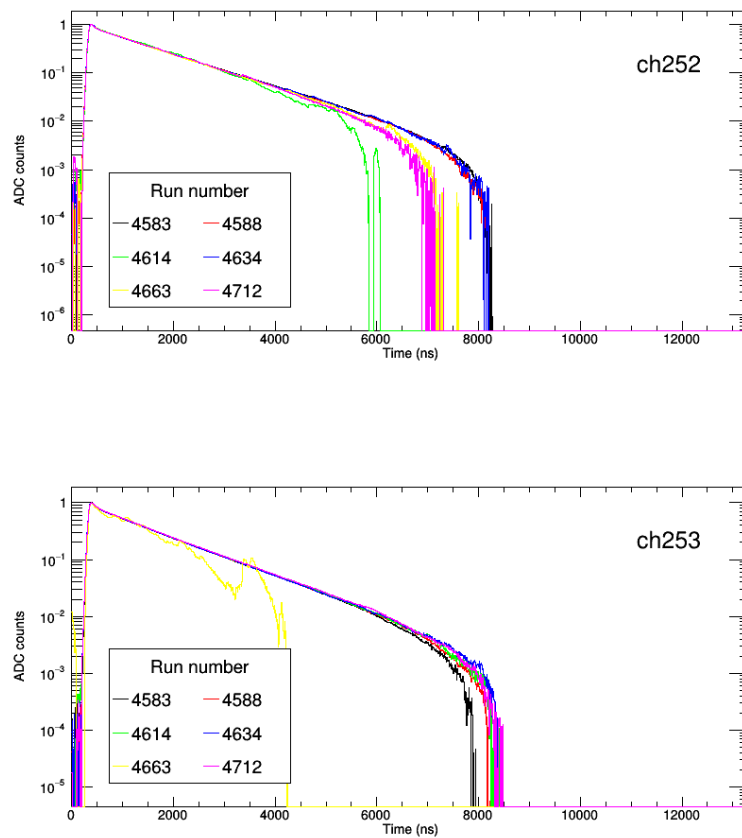
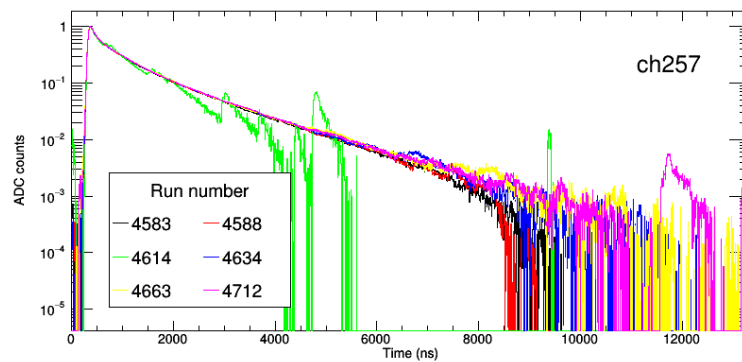


Figure 6.1.2: Average waveform for a double-shifted light guide. DAQ channels 252 and 253.



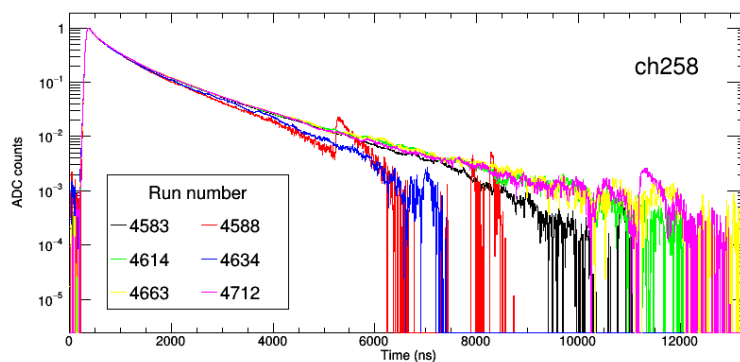


Figure 6.1.3: Average waveform for a dip-coated light guide. DAQ channels 257 and 258.

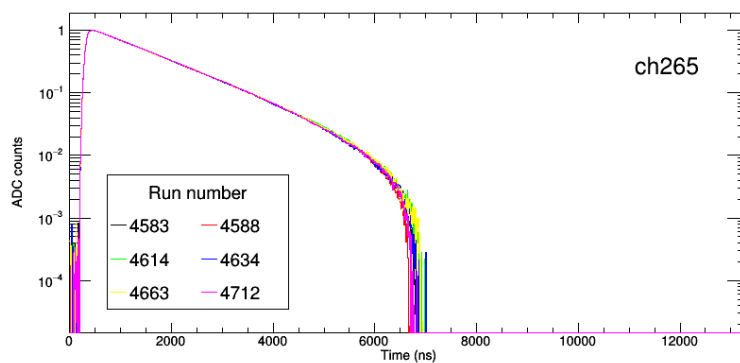
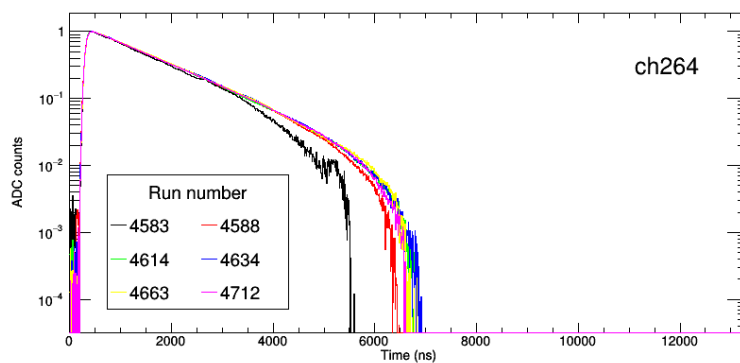


Figure 6.1.4: Average waveform for an ARAPUCA with 6 SiPMs installed in each. DAQ channels 264 and 265.

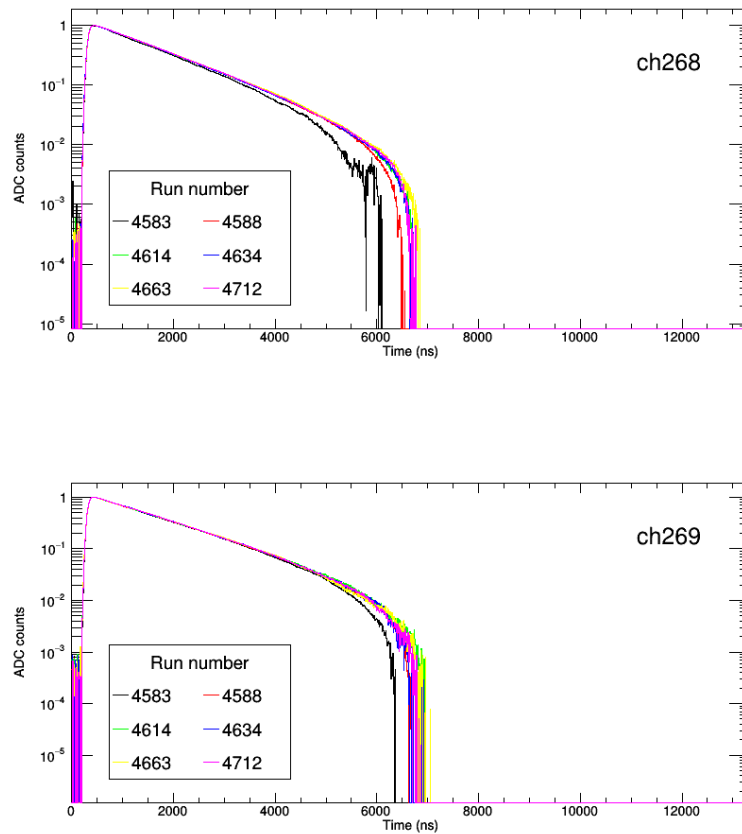


Figure 6.1.5: Average waveform for an ARAPUCA with 12 SiPMs installed in each. DAQ channels 268 and 269.

As mentioned previously, the effect of the undershoot on the signals in ARAPUCA is clear. Still, it was possible to extract the scintillation light slow decay time, as shown in Section 6.1.2.

6.1.2. Slow decay time measurement

After calculating the average waveform, Figures 6.1.2-6.1.5, as described above, a fit was performed by the minimization of a chi-square function with the help of the MINUIT package implemented in the ROOT TMinuit class on the average waveforms for the runs displayed in Table 6.1.

An idealized signal was used for the fit. This idealized signal takes into account that the LAr scintillation light has a fast and a slow decay time component, that the TPB used to shift the light wavelength has a delayed component of scintillation, and that the electronics due to the use of a SiPM introduces a time Gaussian contribution to the final waveform, described in Section 5.4.

The fit was done for each waveform, see Figure 6.1.6. The effect of the undershoot for the ARAPUCA signal is clearly noticed, and this entailed in choosing different time intervals for the fit of each channel. The result of the slow decay time obtained after the fit for all analyzed channels is shown in Figure 6.1.7.

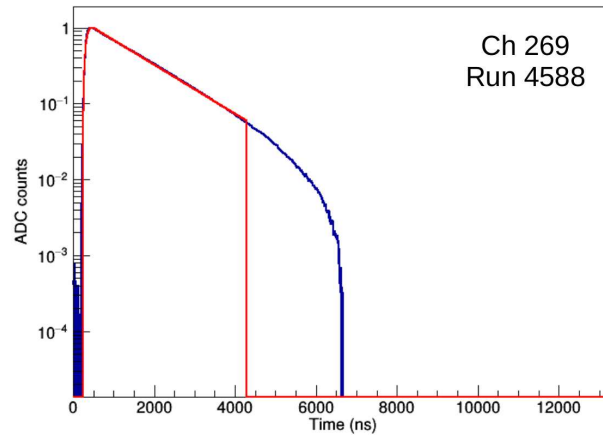


Figure 6.1.6: Fit (red) done on the average waveform (blue) of channel 269 in run 4588.

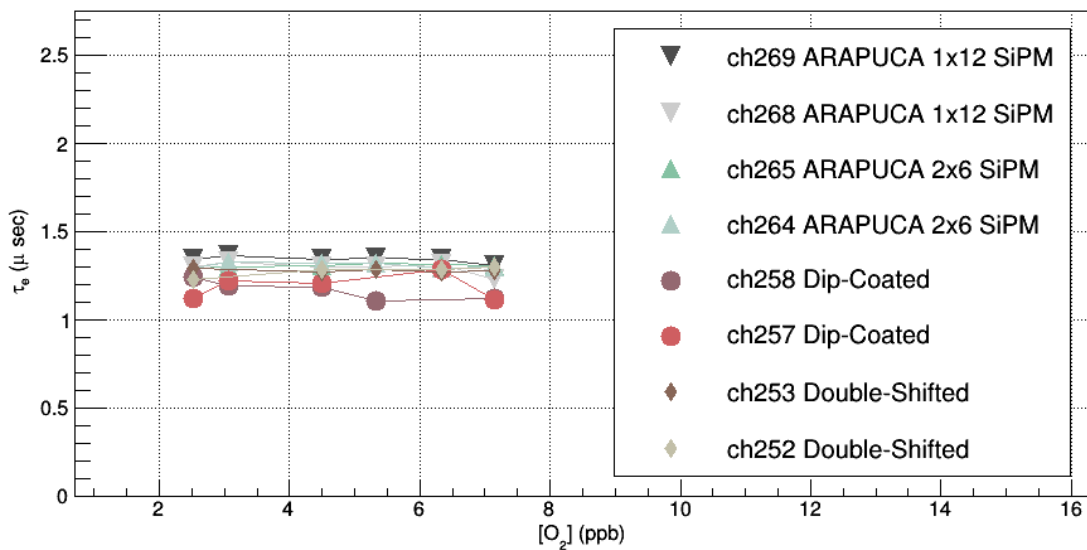


Figure 6.1.7: The LAr scintillation light slow decay time component for some channels in APA 6 of the ProtoDUNE-SP experiment. Channels 252 and 253 are Double-Shifted light guide bars. Channels 257 and 258 are Dip-Coated light guide bars. Channels 264 and 265 (268 and 269) are ARAPUCAs with six (12) SiPMs installed in each..

6.2. Rayleigh scattering analysis

The previous section showed that the shape of the waveform does not change in the purity range presented by the ProtoDUNE-SP experiment. This effect can also be observed in

waveforms from the 0.5 GeV particle beam, as shown in Figure 6.2.2.

The same fit described in the previous section was repeated here for channel 134 for the beam data, and a slow scintillation component of 1,711(1,752) ns was found for the run 4878(5837). In both runs, the 0.5 GeV incident beam, Figure 6.2.1, was mostly composed of electrons meaning that interactions in liquid argon generate shower particles. Since the secondary particles can also interact with liquid argon, there will be some late light in each waveform. This late light might be causing this higher component of slow scintillation for the average waveform when compared to the values found in the previous section. Despite the value for the slow component of scintillation, it remains constant as expected.

The beam runs were selected so that the only difference in configuration was the purity of the liquid argon. Therefore, any difference in the amount of arriving photons can be associated with the Rayleigh scattering and absorption effects. As shown in Table 5.2, both beam runs that were analyzed had a cathode voltage of 180 kV and an ARAPUCA bias voltage of 48 V.

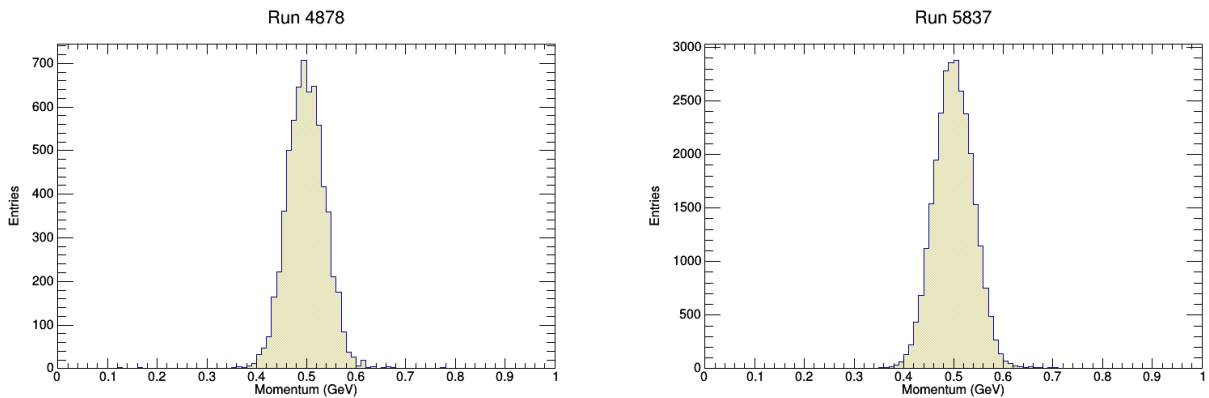


Figure 6.2.1: Beam momentum distribution for beam runs 4878 and 5837.

After verifying the beam instrumentation information and selecting only "good beam events"¹ each one of the 12 ARAPUCA channels was analyzed. To calculate the number of photons arriving at the detector an analysis of individual waveforms was made. An ADC histogram of the first 700 ticks was made for each waveform and the baseline was considered as being the center of a Gaussian fit on this histogram. After subtracting the baseline, an integral of the last 1,300 ticks was made.

¹A beam event is defined as a good beam event if there was information from the particle ID detectors, such as TOF and Cerenkov detector.

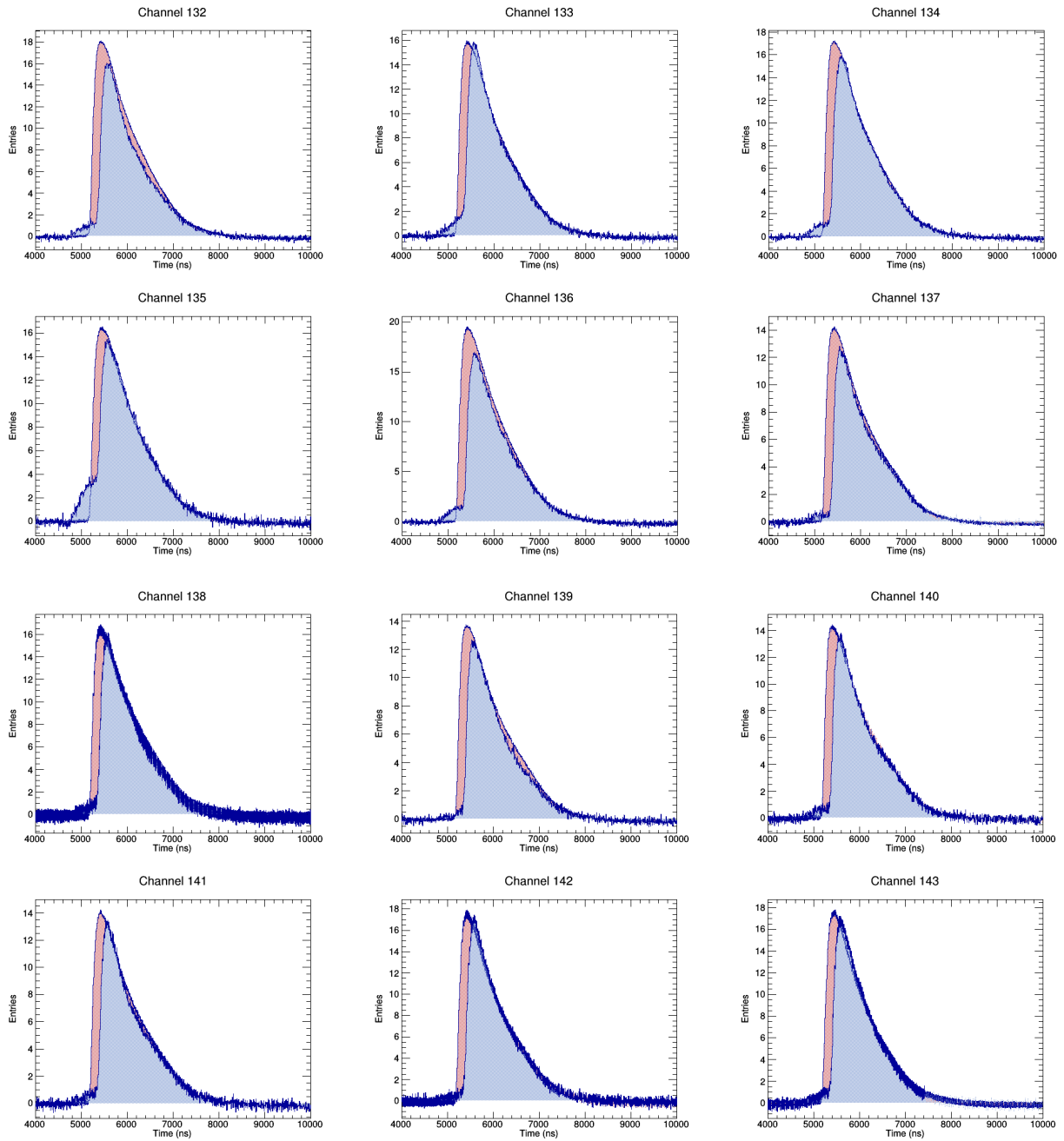


Figure 6.2.2: Average waveforms for a 0.5 GeV beam signal for run 4878 (blue) and run 5837 (red). The average waveform was calculated considering only the pulses of light generated by the beam of particles, disregarding those generated by cosmic rays.

The calibration shown in Table 4.3 represents the integral value for a single photon. Therefore, to recover the amount of detected photons per detector for the beam events, one should divide the total integral by the value of the calibration, as follows:

$$\text{Number of Photons} = \frac{\text{Waveform Integral}}{\text{Calibration}} \quad (6.2.1)$$

By putting in a histogram the number of photons detected by all 12 channels together it

is possible to identify a peak relative to the noise and another relative to the light generated by the beam of particles, Figure 6.2.3.

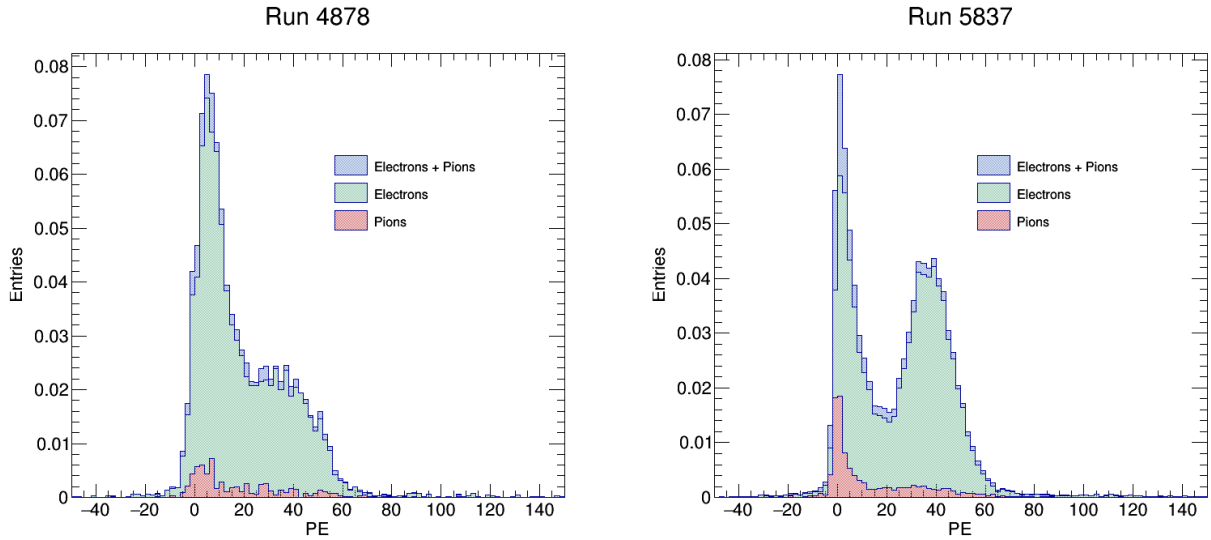


Figure 6.2.3: Total number of photons detected by 12 ARAPUCA channels together for a particle beam of 0.5 GeV. The particle identification was done using both time-of-flight and Cerenkov detector information.

A fit of the sum of two Gaussians

$$f(x) = p_0 \times \exp\left[\frac{-(x-p_1)^2}{2 \times p_2^2}\right] + p_3 \times \exp\left[\frac{-(x-p_4)^2}{2 \times p_5^2}\right] \quad (6.2.2)$$

was made to identify the center of both peaks, as shown in Figure 6.2.4. Substituting in

$$\text{Number of Photons} = p_4 - p_1 \quad (6.2.3)$$

the fit parameters from Figure 6.2.4, it was possible to calculate the number of detected photons for each run. As a result, there were $25 \pm 2(31.9 \pm 0.4)$ photons being detected by the ARAPUCA module in run 4878(5837). Since the only difference between the two runs is the concentration of impurities, the difference in the amount of detected photons can be associated with the Rayleigh scattering and absorption effect.

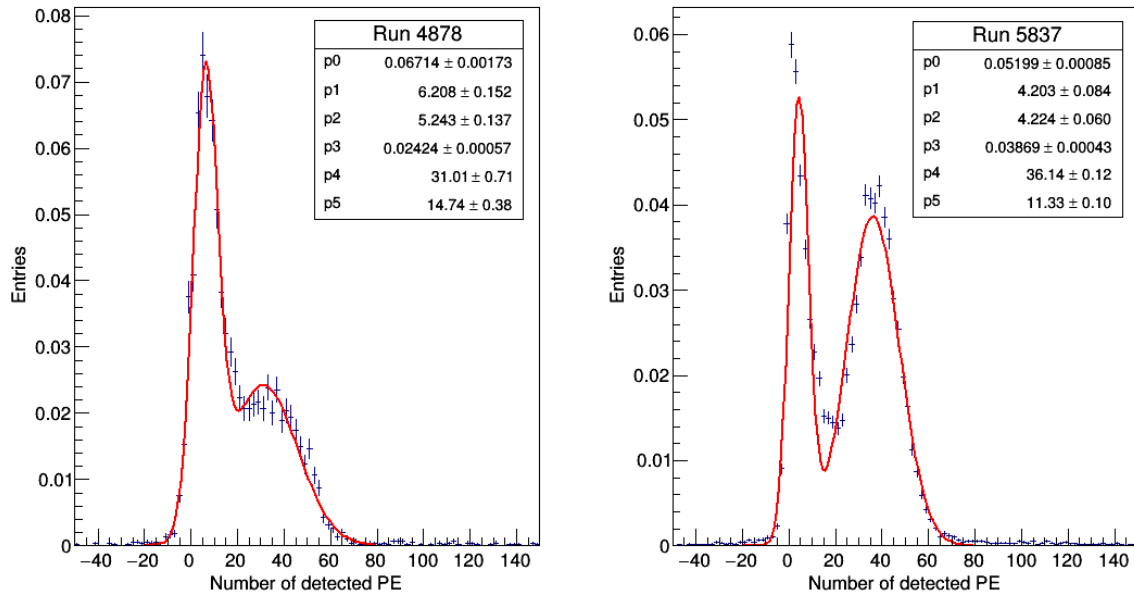


Figure 6.2.4: Fit of two Gaussians on the integral histogram distribution. The peak near zero represents the resulting integrals of empty waveforms, and the second peak represents the resulting integrals of waveforms associated to the beam.

Note that for a 0.5 GeV particle beam, it is not possible to identify the beam peak just by looking at the integral histogram distribution of a single channel, as shown in blue in Figure 6.2.5. It is necessary to sum the contribution of all 12 ARAPUCA channels to be able to distinguish both noise and beam peak.

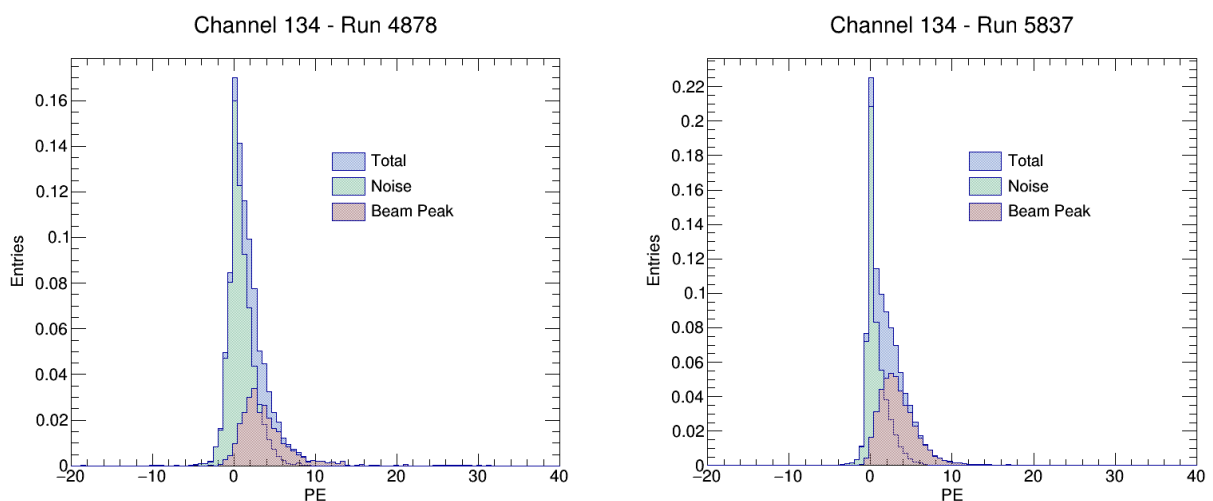


Figure 6.2.5: Number of photons detected by channel 134 for a particle beam of 0.5 GeV.

6.3. Monte Carlo toy model

A toy model of a Monte Carlo simulation was made to "measure" the Rayleigh length. Remember that the volume of the ProtoDUNE-SP experiment is divided by the cathode positioned in the center and parallel to the direction of the particle beam. An electron beam of 0.5 GeV was simulated entering the half of the experiment sensitive to the beam. The direction of the original beam of the experiment was preserved in the simulation.

The trajectory of the particle within the volume of liquid argon was divided into steps of 1 cm. The energy of the beam was updated with each step as

$$\frac{dE}{dx}(E) = f_{\text{Stopping Power}}(E) \times \rho_{Ar} \times d_{\text{step}}, \quad (6.3.1)$$

where $f_{\text{Stopping Power}}(E)$ is the total stopping power distribution of electrons in liquid argon given in Figure 6.3.1, $\rho_{Ar} = 1.4 \text{ g/cm}^3$ is the argon density, and $d_{\text{step}} = 1 \text{ cm}$ is the distance traveled by the particle in each step.

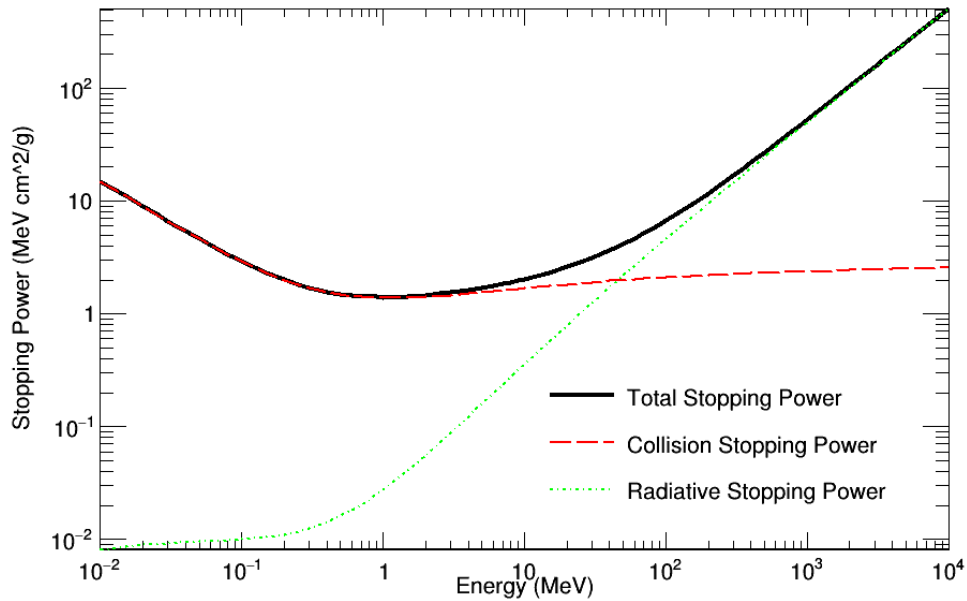


Figure 6.3.1: Stopping power of electrons in liquid argon [40].

The maximum number of photons emitted by liquid argon per deposited energy of 1 MeV can be estimated to be 5.13×10^4 photons/MeV, see Table 2.1, but it is known that the effective light yield depends on mainly two external factors. First, the light yield depends on the particle ID that is crossing the detector and its linear energy transfer (LET). Considering an electron in LAr, the relative scintillation light yield at zero electric field is

$$Y_{rel}^e = 0.8, \quad (6.3.2)$$

as shown in Figure 6.3.2. Hence the absolute yield for minimum ionizing electrons in LAr is

$$Y_{ph}^e = 0.8 \cdot (5.13 \times 10^4 \text{ photons/MeV}) = 4.1 \times 10^4 \text{ photons/MeV}. \quad (6.3.3)$$

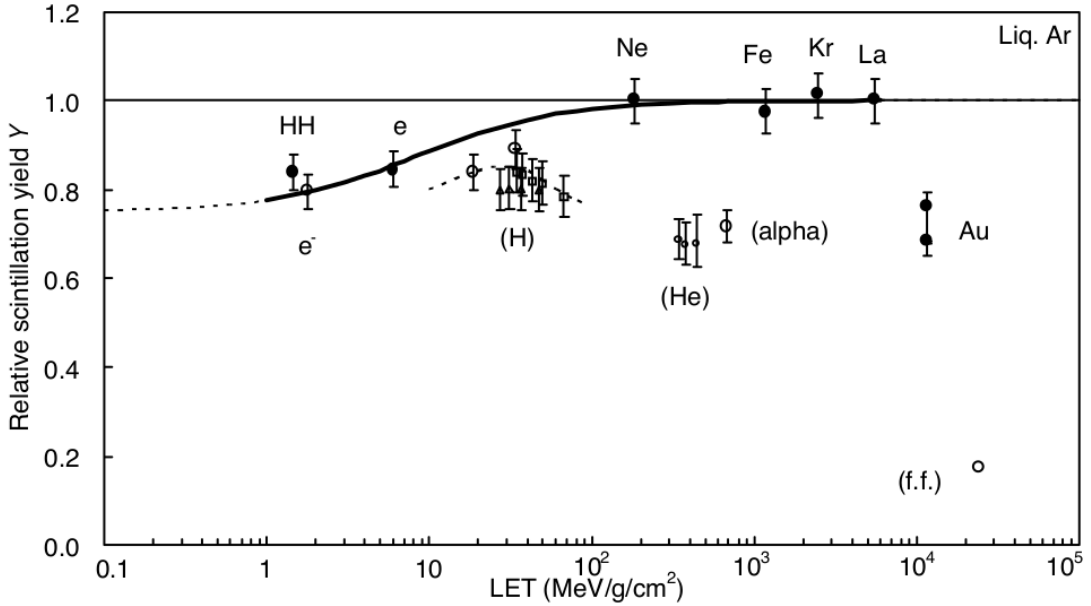


Figure 6.3.2: LET dependence of scintillation yield, Y , in liquid argon. Solid circles show the yields for relativistic particles. Non-relativistic particles are represented by open circles. Open squares and triangles show the yield for non-relativistic protons whereas small open circles show those for non relativistic-helium ions [41].

The second factor depends on the intensity of the electric field applied in the TPC. As explained in Chapter 3, the scintillation process can happen either through the de-excitation of excited Ar atoms or through the recombination of Ar^+ ions and free electrons. The presence of an electric field in the LAr volume can influence the second process preventing ion-electron recombination. Studies were made to understand the dependence of the LAr scintillation yield on the strength of an applied electric field [42] for many types of ionizing radiation. From Figure 6.3.3 it is possible to determine the relative reduction, A_E , in Y_{ph}^e in the presence of an electric field. Since an electric field of 500 V/cm was applied in the ProtoDUNE-SP detector, the recombination factor is

$$A_E(E = 500 \text{ V/cm}) \approx 0.6. \quad (6.3.4)$$

Finally, by multiplying both Equations 6.3.3 and 6.3.4, the absolute scintillation light yield

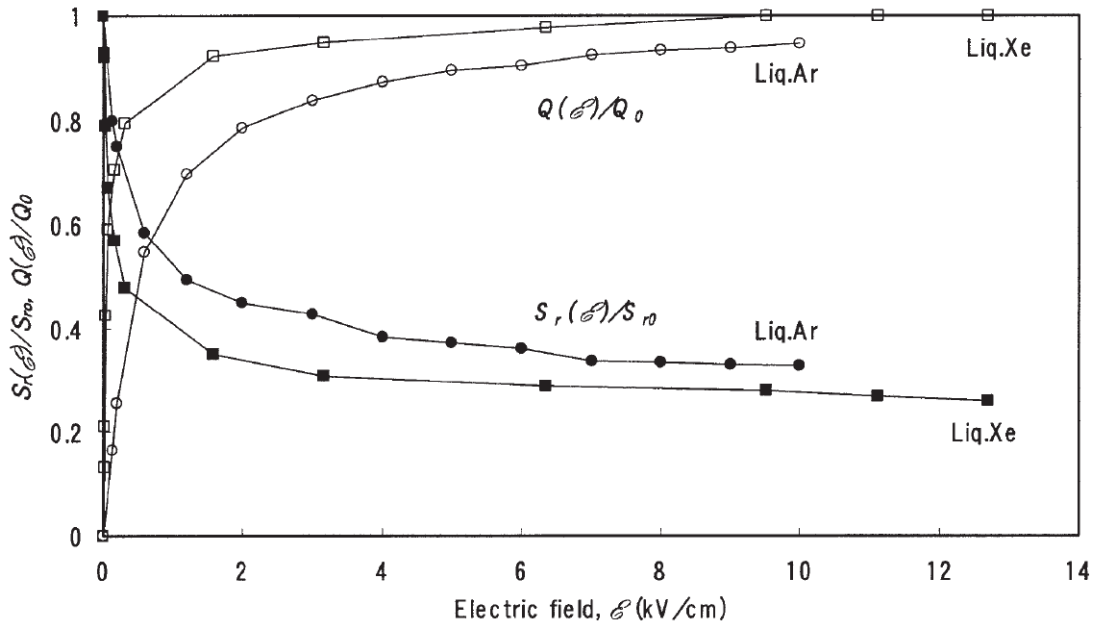


Figure 6.3.3: Saturation curves of ionization (open symbols) and scintillation (close symbols) for 1 MeV electrons in LAr (dots) and in liquid Xenon (squares) as function of the electric field strength [41].

for minimum ionizing electrons in LAr with an applied electric field of 500 V/cm can be estimated to be:

$$Y_{ph}^e(E = 500 \text{ V/cm}) \approx 2.4 \times 10^4 \text{ photons/MeV} \quad (6.3.5)$$

The simulation of the scintillation light is made in two steps. First, the amount of energy lost in each step of 1 cm is calculated according to Equation 6.3.1. Second $dE/dx \times 2.4 \times 10^3$ photons are generated isotropically at the final position of each step of 1 cm. Note that an amount of produced photons ten times smaller than the real one was simulated to make the simulation faster, and this value is corrected in the calculation of the amount of detected photons, Equation 6.3.7.

After being generated, each photon can hit a wall, be absorbed, or be scattered. Therefore three distances are analyzed for each photon. By knowing where the photon was generated and its direction, it is possible to calculate the distance to be traveled until it hits a wall, d_{wall} . The distance to be travelled until an absorption, d_{abs} , or scattering, d_{scat} , obeys the following exponential distribution of probability

$$P(x) = \frac{1}{\lambda} e^{-x/\lambda}, \quad (6.3.6)$$

where λ is either the absorption length, given by Equation 3.1.5, or the Rayleigh scattering length. Since the idea is to reproduce the results presented in the previous section, a simulation using the absorption length for runs 4878 and 5837 was made using 13 different Rayleigh scattering lengths (10, 20, 30, 40, 50, 60, 70, 80, 90, 100, 200, 500, and 1000 cm) each time. The shortest distance among d_{wall} , d_{abs} , and d_{scat} , indicates the predominant effect, which means that

- if $d_{wall} \leq d_{abs}$ and $d_{wall} \leq d_{scat}$, the photon is going to hit the wall before being either absorbed or scattered. In this case, if the photon hits the ARAPUCA module installed on the APA 3, it sums one in the detected photon count, otherwise it is ignored;
- else if $d_{abs} < d_{wall}$ and $d_{abs} \leq d_{scat}$, the photon is going to be absorbed before either hitting the wall or being scattered. In this case, this photon is also ignored;
- lastly, if $d_{scat} < d_{wall}$ and $d_{scat} < d_{abs}$, the photon is going to be scattered before either hitting the wall or being absorbed. In this case, another random direction is associated to the scattering point and all the process is repeated until the photon is either absorbed or detected.

The output of this simulation is the number of photons that reached the ARAPUCA module. The number of detected photons can be calculated as

$$n_{\text{detected}} = n_{\text{incident}}^{\text{sim}} \times 10 \times T_{\text{APA}} \times \epsilon_{\text{ARAPUCA}}, \quad (6.3.7)$$

where $n_{\text{incident}}^{\text{sim}}$ is the number of photons that reached the ARAPUCA module given by the simulation, the factor 10 corrects the amount of generated photons, $T_{\text{APA}} \sim 0.7$ [13] is the transparency of the APA², and $\epsilon_{\text{ARAPUCA}} \sim (1.0 \pm 0.1)\%$ is the detection efficiency of ARAPUCA. The simulation for each Rayleigh scattering length was made ten times, and the standard deviation, $\delta n_{\text{incident}}^{\text{sim}}$, was calculated as

$$\delta n_{\text{incident}}^{\text{sim}} = \sqrt{\frac{\sum_{i=1}^N (n_i - \bar{n})^2}{N}} \quad (6.3.8)$$

where n_i is the output of the each simulation, and \bar{n} is the average number of incident photons among $N = 10$ simulations made. The final result is shown in Figure 6.3.4. Small scattering distances imply a greater probability of scattering, consequently, the photon travels a

²Remember that the photon-detection system is installed behind the APA, which causes the photon to cross the APA frame before actually reaching the detector.

larger distance until it is detected, as shown in Figure 6.3.5. As a new scattering and absorption distance is calculated for each interaction, more interactions occur, greater the probability that the photon will be absorbed by the medium.

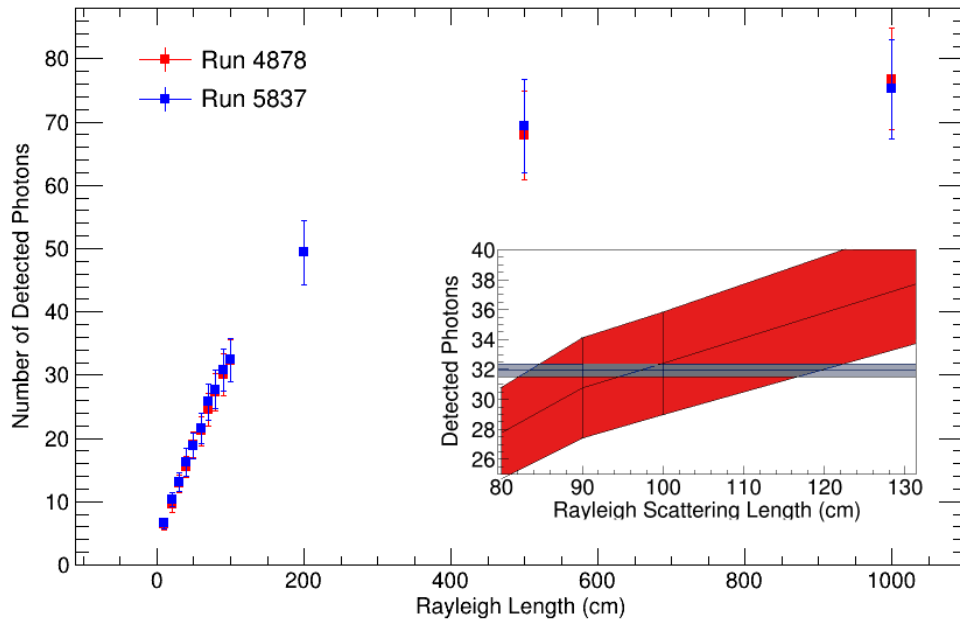


Figure 6.3.4: Number of simulated photons detected by the ARAPUCA module for different Rayleigh scattering lengths. The smaller the Rayleigh scattering length, the smaller is the quantity of photons arriving at the detector due to the greater probability of absorption along the track. From the interception of the band of detected photons given by the simulation (red) and the band of measured detected photons for run 5837 given by Figure 6.2.4 (gray), it was possible to measure a Rayleigh scattering length of 97^{+25}_{-15} cm.

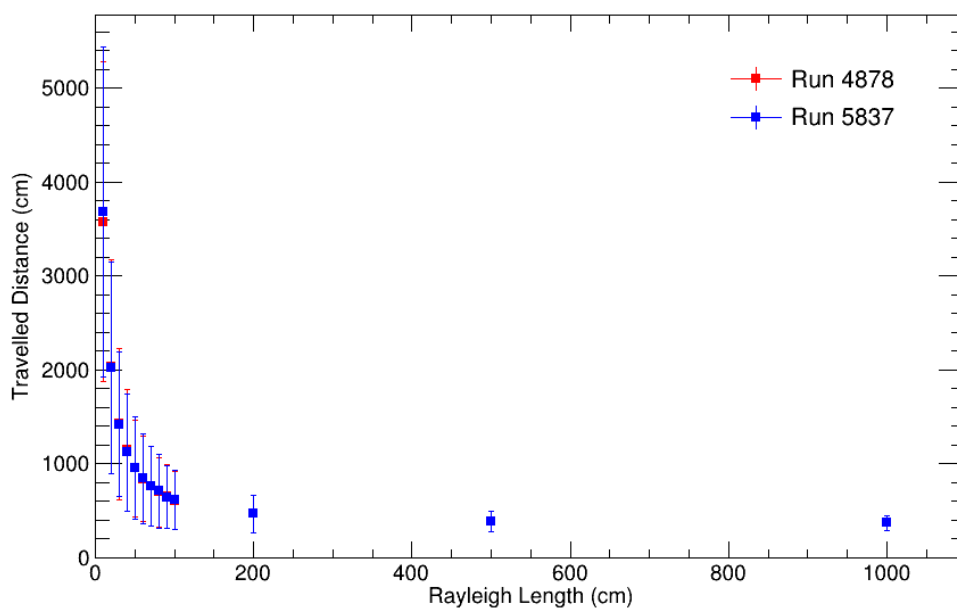


Figure 6.3.5: Distance travelled by the photon until its detection by the ARAPUCA module for different Rayleigh scattering lengths.

From the data analysis presented in the previous section it was found that $25 \pm 2 (31.9 \pm 0.4)$ photons were detected by the ARAPUCA module for run 4878(5837). However, the simulation described in this section does not show distinct behaviors for the purity levels of the analyzed runs, see Figure 6.3.4. Setting the value of Rayleigh scattering length found for run 5837 as 97_{-15}^{+25} cm, a scan through different absorption lengths was done to explore in which limit an amount of ~ 25 detected photons is recovered. As shown in Figure 6.3.6, it would be necessary to have an absorption length of 2415_{-897}^{+2639} cm to detect the desired number of photons.

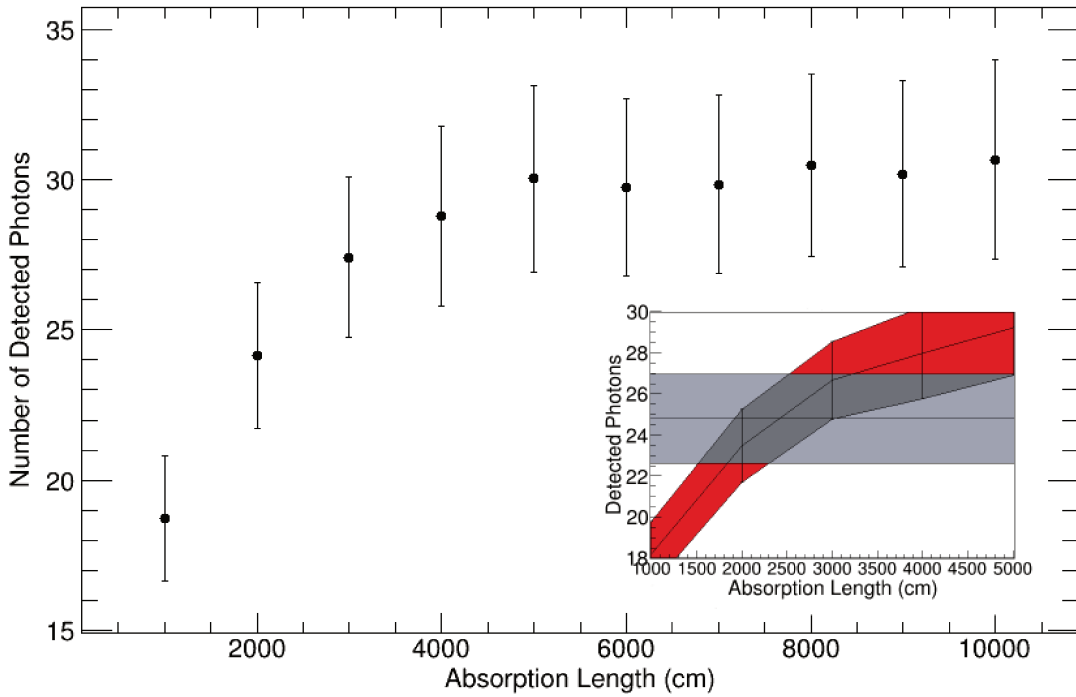


Figure 6.3.6: Number of detected photons for different absorption lengths, for a fixed Rayleigh scattering length of 97 cm. From the interception of the band of detected photons given by the simulation (red) and the band of measured detected photons for run 4878 given by Figure 6.2.4 (gray), it was possible to measure an absorption length of 2415_{-897}^{+2639} cm.

Table 6.3: Summary of important information used in the Monte Carlo toy model described in this section.

Absolute LAr light yield	$\sim 2.4 \times 10^4$ photons/MeV
Beam energy	0.5 GeV
Relative scintillation light	80%
Recombination factor	60%
Absorption length	$l_A(4878) \sim 540$ m and $l_A(5837) \sim 5$ km
Absorption coefficient	$k_a = 0.034 \text{ ppm}^{-1} \text{ cm}^{-1}$
TPC dimensions	360 (width) \times 600 (height) \times 720 (length) cm^3

Chapter 7

Conclusions

The data analysis for the ProtoDUNE-SP has shown coincidences between pulses of light with self-trigger and beam trigger. Besides, a theoretical consistency was found in the signal from liquid argon scintillation light over the data acquisition period. This indicates proper operation of the light detection system, including the ARAPUCAs.

A careful calibration of the light detectors was successfully done using two distinct methods described in Section 4.4. Both methods used light from a pulsed LED to obtain the single photo-electron charge and the crosstalk factor of the SiPMs. The agreement between the two methods indicates the reliability of the results, which led to a final refined correction in which silicon photomultiplier crosstalk effects were considered allowing the determination of the amount of light detected.

To properly use the scintillation light, one should verify the purity level of the liquid argon since the behavior of the light may undergo changes due to the presence of impurities in the active medium of the detector. A description of these effects was given in Chapter 3, showing that different slow-decay times may occur in combination with Rayleigh scattering and absorption effects that will change the amount of light that arrived at the light detector.

The present work considered the fast and slow responses of scintillation light together with the delayed response of TPB, added to the response of the SiPMs to obtain the slow-decaytime, as shown in Section 5.2.3. The result of $\sim 1.275 \mu\text{s}$ confirms the constant slow-decay time predicted by the WArP collaboration for a concentration below 0.1 ppm. This result was found among all three different light detectors during the beginning of the data acquisition period, in which impurity concentration was the highest. Therefore, it is possible to assume that no quenching effect is observed during the period of operation of the ex-

periment of the dimensions of the ProtoDUNE-SP since purification pumps started to work decreasing the concentration of impurities.

A first attempt to analyze the number of detected photons was made using self-triggered signals, with a threshold of 200 ADC, the value used during most of the data taking. However, it has been found (Section 5.2.1) that a threshold of 200 ADC is large enough to cut off the distribution of the detected signal. Consequently, beam data was used to analyze the number of detected photons by the ARAPUCA array installed at APA 3, close to the beam entry point. A waveform was saved by all photosensitive devices for each beam trigger. The number of detected photons was calculated by dividing the integral of the pulse by the calibration of each channel. For a 0.5 GeV particle beam, the integral of the signal detected by a single channel, see Figure 6.2.5, was not large enough to be distinguishable from the baseline integral peak, and for this reason it was necessary to sum the contribution of all 12 ARAPUCA channels, see Figure 6.2.3, to be able to recover a baseline peak and a beam peak.

From a two-Gaussian fit in the pulse integral distribution, it was measured that run 4878 detected 25 ± 2 photons, and run 5837 detected 31.9 ± 0.4 photons. The difference in the number of detected photons was initially supposed to be associated with absorption and Rayleigh scattering effects.

A Monte Carlo toy model was developed to verify this assumption. In the model described in Section 6.3, photons emitted along the trajectory of the 0.5 GeV electron beam could be Rayleigh scattered, absorbed by the medium and wall, or be detected by the ARAPUCA module. The result obtained in the simulation has revealed that both runs would detect the same amount of photons for a fixed Rayleigh scattering length. The Rayleigh scattering length found for run 5837 of 97^{+25}_{-15} cm was fixed to try to reproduce the result found in the data analysis for run 4878, and a scan through different absorption lengths was done. It was found that an absorption length of 2415^{+2639}_{-897} cm would be necessary to result in the 25 ± 2 photons detected in run 4878. This result, however, does not completely agree with the absorption length of $\sim 54,000$ cm theoretically calculated from the electron lifetime, Equation 3.1.5.

The discrepancy between the calculated absorption length and the simulated one can be due to a couple of factors. First, although less likely, the toy model is too simplified for the proposed simulation. Second, the calculation of the absorption length given by Equation

3.1.5 is not valid for experiments of the proportion of the ProtoDUNE-SP experiment. Third, the number of beam events recorded during run 4878 was not enough to form a beam peak as clear as the one for run 5837, leading to a wrong fit value. A more complete Monte Carlo simulation would be necessary to prove the first hypothesis. More studies in large LArTPCs could prove the second hypothesis. Finally, this analysis could be repeated for other runs in conditions similar to the runs analyzed in this work, to check the values found. Even though the calculated absorption length does not recover the measured number of photons for run 4878, a satisfactory Rayleigh scattering length was found for run 5837 together with the behavior of light previously predicted in Section 3.1.3, proving the knowledge in liquid argon scintillation and the validity of the toy model simulation.

Bibliography

1. Turck-Chièze, S. The Standard Solar Model and beyond. *Journal of Physics: Conference Series* **665**, P012078 (2016). DOI: [10.1088/1742-6596/665/1/012078](https://doi.org/10.1088/1742-6596/665/1/012078).
2. Dar, A. Solar Neutrinos and the Standard Solar Model (1997). arXiv: [astro-ph/9707015](https://arxiv.org/abs/astro-ph/9707015).
3. Davis, R. A Review of the Homestake Solar Neutrino Experiment. *Progress in Particle and Nuclear Physics* **32**, 13-32 (1994). DOI: [10.1016/0146-6410\(94\)90004-3](https://doi.org/10.1016/0146-6410(94)90004-3).
4. Dore, U. & Zanello, L. Bruno Pontecorvo and neutrino physics (2009). arXiv: [0910.1657](https://arxiv.org/abs/0910.1657) [[physics.hist-ph](https://arxiv.org/archive/physics)].
5. Thomson, M. *Modern Particle Physics*. Cambridge University Press, 2013.
6. Giunti, C. & Kim, C. W. *Fundamentals of Neutrino Physics and Astrophysics*. Oxford University Press, 2007.
7. Patrignani, C. *et al.* Review of Particle Physics. *Chin. Phys.* **C40**, P100001 (2016). DOI: [10.1088/1674-1137/40/10/100001](https://doi.org/10.1088/1674-1137/40/10/100001).
8. Nunokawa, H., Parke, S. & Valle, J. W. F. CP Violation and Neutrino Oscillations. *Progress in Particle and Nuclear Physics* **60**, 338-402 (2007). DOI: [10.1016/j.ppnp.2007.10.001](https://doi.org/10.1016/j.ppnp.2007.10.001).
9. Gratieri, D. R., Guzzo, M. M. & Peres, O. L. G. Impact of standard neutrino oscillations and systematics in proton lifetime measurements (2017). arXiv: [1704.03927](https://arxiv.org/abs/1704.03927) [[hep-ph](https://arxiv.org/archive/hep)].
10. Janka, H. -Th. Neutrino Emission from Supernovae. *Handbook of Supernovae* (2017). DOI: [10.1007/978-3-319-21846-5_4](https://doi.org/10.1007/978-3-319-21846-5_4).
11. B. Abi *et al.* The DUNE Far Detector Interim Design Report Volume 1: Physics, Technology and Strategies (2018). arXiv: [1807.10334](https://arxiv.org/abs/1807.10334) [[physics.ins-det](https://arxiv.org/archive/physics)].

12. B. Kayser. Tensions with the Three-Neutrino Paradigm. *Proceedings of the 47th Rencontres de Moriond on Electroweak Interactions and Unified Theories*, pp. 191-196 (2012). arXiv: [1207.2167](https://arxiv.org/abs/1207.2167) [hep-ph].
13. B. Abi *et al.* The DUNE Far Detector Interim Design Report Volume 2: Single-Phase Module (2018). arXiv: [1807.10327](https://arxiv.org/abs/1807.10327) [physics.ins-det].
14. B. Abi *et al.* The DUNE Far Detector Interim Design Report Volume 3: Dual-Phase Module (2018). arXiv: [1807.10340](https://arxiv.org/abs/1807.10340) [physics.ins-det].
15. Adams, C. *et al.* Ionization electron signal processing in single phase LArTPCs. Part I. Algorithm Description and quantitative evaluation with MicroBooNE simulation. *JINST* **13**, P07006 (2018). DOI: [10.1088/1748-0221/13/07/P07006](https://doi.org/10.1088/1748-0221/13/07/P07006).
16. Rubbia, C. The Liquid Argon Time Projection Chamber: A New Concept For Neutrino Detectors. *European Organization for Nuclear Research, EP Internal Report 77-8* (1977).
17. *MicroBooNE experiment*. URL: <https://microboone.fnal.gov/> (visited on 2019).
18. Walkowiak, W. Drift velocity of free electrons in liquid argon. *Nuclear Instruments and Methods in Physics Research Section A: Accelerators, Spectrometers, Detectors and Associated Equipment* **449**, 288-294 (2000). DOI: [10.1016/S0168-9002\(99\)01301-7](https://doi.org/10.1016/S0168-9002(99)01301-7).
19. Heindl, T., Dandl, T., Hofmann, M., Krücken, R., Oberauer L., Potzel, W., Wieser, J. & Ulrich, A. The scintillation of liquid argon. *EPL (Europhysics Letters)* **91**, P62002 (2010). DOI: [10.1209/0295-5075/91/62002](https://doi.org/10.1209/0295-5075/91/62002).
20. Morikawa, E., Reininger, R., Gürtler, P., Saile, V. & Laporte, P. Argon, krypton, and xenon excimer luminescence: From the dilute gas to the condensed phase. *The Journal of Chemical Physics* **91**, 1469-1477 (1989). DOI: [10.1063/1.457108](https://doi.org/10.1063/1.457108).
21. Bakale, G., Sowada, U. & Schmidt, W. F. Effect of an electric field on electron attachment to sulfur hexafluoride, nitrous oxide, and molecular oxygen in liquid argon and xenon. *The Journal of Physical Chemistry* **80**, 2556-2559 (1976). DOI: [10.1021/j100564a006](https://doi.org/10.1021/j100564a006).
22. Acciarri, R. *et al.* Oxygen contamination in liquid Argon: combined effects on ionization electron charge and scintillation light. *Journal of Instrumentation* **5**, P05003 (2010). DOI: [10.1088/1748-0221/5/05/p05003](https://doi.org/10.1088/1748-0221/5/05/p05003).
23. Landau, L. D. & Lifshitz, E. M. *Electrodynamics of Continuous Media*. Oxford, 1984.

24. Seidel, G. M., Lanou, R. E. & Yao, W. Rayleigh scattering in rare-gas liquids. *Nuclear Instruments and Methods in Physics Research Section A: Accelerators, Spectrometers, Detectors and Associated Equipment* **489**, 189-194 (2002). DOI: [10.1016/S0168-9002\(02\)00890-2](https://doi.org/10.1016/S0168-9002(02)00890-2).
25. Baldini, G. Ultraviolet Absorption of Solid Argon, Krypton, and Xenon. *Phys. Rev.* **128**, 1562-1567 (1962). DOI: [10.1103/PhysRev.128.1562](https://doi.org/10.1103/PhysRev.128.1562).
26. Huffman, R. E., Tanaka, Y. & Larrabee, J. C. Absorption Coefficients of Krypton in the 600 to 886 Å Wavelength Region. *Appl. Opt.* **2**, 947-953 (1963). DOI: [10.1364/AO.2.000947](https://doi.org/10.1364/AO.2.000947).
27. Chepel, V. & Araújo, H. Liquid noble gas detectors for low energy particle physics. *Journal of Instrumentation* **8**, R04001–R04001 (2013). DOI: [10.1088/1748-0221/8/04/r04001](https://doi.org/10.1088/1748-0221/8/04/r04001).
28. B. Abi et al. The Single-Phase ProtoDUNE Technical Design Report (2017). arXiv: [1706.07081](https://arxiv.org/abs/1706.07081) [physics.ins-det].
29. Machado, A. A. & Segreto, E. ARAPUCA a new device for liquid argon scintillation light detection. *Journal of Instrumentation* **11**, C02004 (2016). DOI: [10.1088/1748-0221/11/02/c02004](https://doi.org/10.1088/1748-0221/11/02/c02004).
30. *Edmund Optics*. URL: <http://www.edmundoptics.com> (visited on 2019).
31. Gallego, L., Rosado, J., Blanco, F. & Arqueros, F. Modeling crosstalk in silicon photomultipliers. *Journal of Instrumentation* **8**, P05010 (2013). DOI: [10.1088/1748-0221/8/05/p05010](https://doi.org/10.1088/1748-0221/8/05/p05010).
32. Rosado, J. & Hidalgo, S. Characterization and modeling of crosstalk and afterpulsing in Hamamatsu silicon photomultipliers. *Journal of Instrumentation* **10**, P10031 (2015). DOI: [10.1088/1748-0221/10/10/p10031](https://doi.org/10.1088/1748-0221/10/10/p10031).
33. Anderson, J. T., Lurgio, P., Djurcic, Z., Drake, G., Kreps, A. & Oberling, M. *SiPM Signal Processor User Manual*. Version 2.07. Argonne National Laboratory. July 2016.
34. Condat, L. A direct algorithm for 1D total variation denoising. **20**, 1054-1057 (2013).
35. Arneodo, F., Bernardini, E., Cavanna, F., Mitri, I., Ferella, A., Haag, A., Mazza, D., Palamara, O., Piano Mortari, G. B. & Tatananni, E. Electron Lifetime and Purity Monitor for the ICARUS T600 Detector (2007).

36. Segreto, E., Machado, A. A., Paulucci, L., Marinho, F., Galante, D., Guedes, S., Fauth, A., Teixeira, V., Gelli, B., Reggiani-Guzzo, M., Araujo, W., Ambrósio, C., Bissiano, M. & Lixandrão Filho, A. L. Liquid argon test of the ARAPUCA device. *Journal of Instrumentation* **13**, P08021 (2018). DOI: [10.1088/1748-0221/13/08/p08021](https://doi.org/10.1088/1748-0221/13/08/p08021).
37. Fauth, A. C., Penereiro, J. C., Kemp, E., Grizolli, W. C., Consalter, D. M. & Gonzalez, L. F. G. Demonstração experimental da dilatação do tempo e da contração do espaço dos múons da radiação cósmica. *Revista Brasileira de Ensino de Física* **29**, 585-591 (2007). DOI: [10.1590/S1806-11172007000400017](https://doi.org/10.1590/S1806-11172007000400017).
38. Cecchini, S. & Spurio, M. Atmospheric muons: experimental aspects (2012). arXiv: [1208.1171](https://arxiv.org/abs/1208.1171) [astro-ph.EP].
39. Segreto, E. Evidence of delayed light emission of tetraphenyl-butadiene excited by liquid-argon scintillation light. *Phys. Rev. C* **91**, P035503 (2015). DOI: [10.1103/PhysRevC.91.035503](https://doi.org/10.1103/PhysRevC.91.035503).
40. *National Institute of Standards and Technology (NIST) - ESTAR*. URL: <https://physics.nist.gov/PhysRefData/Star/Text/ESTAR.html> (visited on 2019).
41. Kubota, S., Nakamoto, A., Takahashi, T., Hamada, T., Shibamura, E., Miyajima, M., Masuda, K. & Doke, T. Recombination luminescence in liquid argon and in liquid xenon. *Phys. Rev. B* **17**, 2762-2765 (1978). DOI: [10.1103/PhysRevB.17.2762](https://doi.org/10.1103/PhysRevB.17.2762).
42. Doke, T., Hitachi, A., Kikuchi, J., Masuda, K., Okada, H. & Shibamura, E. Absolute Scintillation Yields in Liquid Argon and Xenon for Various Particles. *Japanese Journal of Applied Physics* **41**, 1538-1545 (2002). DOI: [10.1143/jjap.41.1538](https://doi.org/10.1143/jjap.41.1538).